

Impact of Variations in Upper-Level Shear on Simulated Supercells

ROBERT A. WARREN

School of Earth, Atmosphere and Environment, Monash University, Melbourne, Victoria, Australia

HARALD RICHTER

Research and Development Branch, Bureau of Meteorology, Melbourne, Victoria, Australia

HAMISH A. RAMSAY

*School of Earth, Atmosphere and Environment, and ARC Centre of Excellence for Climate System Science,
Monash University, Melbourne, Victoria, Australia*

STEVEN T. SIEMS AND MICHAEL J. MANTON

School of Earth, Atmosphere and Environment, Monash University, Melbourne, Victoria, Australia

(Manuscript received 25 October 2016, in final form 7 March 2017)

ABSTRACT

It has previously been suggested, based on limited observations, that vertical wind shear in the upper troposphere is a key control on supercell morphology, with the low-precipitation, high-precipitation, and classic archetypes favored under strong, weak, and moderate shear, respectively. The idea is that, with increasing upper-level shear (ULS), hydrometeors are transported farther from the updraft by stronger storm-relative anvil-level winds, limiting their growth and thereby reducing precipitation intensity. The present study represents the first attempt to test this hypothesis, using idealized simulations of supercells performed across a range of 6–12-km shear profiles.

Contrary to expectations, there is a significant increase in surface precipitation and an associated strengthening of outflow winds as ULS magnitude is increased from 0 to 20 m s^{-1} . These changes result from an increase in storm motion, which drives stronger low-level inflow, a wider updraft, and enhanced condensation. A further increase in ULS magnitude to 30 m s^{-1} promotes a slight reduction in storm intensity associated with surging rear-flank outflow. However, this transition in behavior is found to be sensitive to other factors that influence cold-pool strength, such as mixed-layer depth and model microphysics. Variations in the vertical distribution and direction of ULS are also considered, but are found to have a much smaller impact on storm intensity than variations in ULS magnitude.

Suggestions for the disparity between the current results and the aforementioned observations are offered and the need for further research on supercell morphology—in particular, simulations in drier environments—is emphasized.

1. Introduction

The seminal numerical modeling studies of Weisman and Klemp (1982, 1984) demonstrated the critical role that vertical wind shear plays in the organization of deep, moist convection. In particular, they showed that increasing shear promotes a transition in storm mode from short-lived single cells to multicell clusters and,

ultimately, to supercells. This transition is typically explained in terms of three key changes in the storm-scale flow (e.g., Markowski and Richardson 2010, chapter 8). The first is increasing separation of the storm updraft and downdraft by means of the downshear advection of growing hydrometeors. The second is an increase in low-level storm-relative (SR) flow that prevents negatively buoyant outflow air from undercutting the updraft. The third is the development of vertical perturbation pressure gradient accelerations (VPPGAs) in association with vertical vorticity (formed via the tilting and stretching of horizontal

Corresponding author: Robert A. Warren, rob.warren@monash.edu

vorticity by the updraft) and the so-called updraft-in-shear effect (Rotunno and Klemp 1982). In supercells, these accelerations contribute significantly to updraft strength, particularly at low levels (Weisman and Klemp 1984), and give rise to the characteristic deviant motion of these storms relative to the mean flow (Rotunno and Klemp 1985; Davies-Jones 2002).

Weisman and Klemp primarily considered shear below about 6 km and subsequent idealized modeling studies have largely done the same (e.g., Weisman and Rotunno 2000; James and Markowski 2010; Nowotarski et al. 2011; Verrelle et al. 2015; Hastings and Richardson 2016). Shear in the first few kilometers above the surface is particularly relevant to supercells because it determines the horizontal vorticity of air ingested by the storm and thus the strength of the low-level mesocyclone (Coffer and Parker 2015). This, in turn, strongly influences the potential for tornadogenesis, which seems to require strong dynamic lifting near cloud base (Markowski and Richardson 2014). However, upper-level shear (ULS), defined here as the shear above 6 km, has also been suggested to modulate the likelihood of severe weather via its effect on supercell morphology (Rasmussen and Straka 1998, hereinafter RS98).

Observed supercells are typically classified into one of three types based on the intensity and updraft-relative distribution of their associated precipitation (Doswell et al. 1990; Moller et al. 1994; RS98; Beatty et al. 2008). Classic (CL) supercells are characterized by intense precipitation in the forward-flank region, with some rain and possibly hail wrapping around the mesocyclone to produce the familiar hook-echo signature in radar imagery (Browning 1964; Lemon and Doswell 1979). Low-precipitation (LP) supercells feature little to no rainfall in close proximity to the updraft and, therefore, generally lack a hook echo, while light to moderate rain and large hail may fall ahead of the storm from the anvil (Bluestein and Parks 1983; Bluestein 1984). At the other end of the spectrum, high-precipitation (HP) supercells are characterized by significant precipitation around the updraft and mesocyclone, giving them a kidney bean shape in radar imagery (Moller et al. 1990). Studies suggest that the three types of supercell differ in their propensity to produce particular hazards (Doswell et al. 1990; Moller et al. 1994). For example, CL storms are the most prolific tornado producers, while LPs are rarely tornadic but can produce large hail. HPs are less likely than CLs to spawn strong (EF 2–3) and violent (EF 4–5) tornadoes, but can produce flash flooding, large hail, and damaging outflow winds. These differences have motivated research into environmental controls on supercell morphology.

RS98 classified 43 isolated supercells as CL, LP, or HP and then compared their environments using

representative proximity soundings. The most striking difference they identified was in the wind shear above 7 km, with LP and HP storms being associated with the strongest and weakest shear, respectively, and CL storms falling in between (their Figs. 6 and 7). Their composite LP hodograph also featured notable backing of the flow at upper levels while the equivalent hodograph for HPs showed slight veering. The average storm motion for CLs and LPs was found to be comparable, while HPs moved slightly faster. Together, these differences suggest that upper-level SR flow increases across the supercell spectrum from HP to LP. RS98 argued that this factor could explain the differences in precipitation intensity and distribution between the morphologies via its effects on hydrometeor advection within the storm's anvil. Specifically, they hypothesized that in environments with strong upper-level SR flow, hydrometeors descending from the forward anvil are displaced farther from the updraft and thus are less likely to be reingested by it. This limits their growth, promoting weak precipitation concentrated primarily in the storm's forward flank (i.e., an LP storm). Conversely, in environments with weak upper-level SR flow, hydrometeors descend in close proximity to the updraft and thus are more readily recycled, leading ultimately to more intense precipitation, which wraps around the mesocyclone (i.e., an HP storm). Earlier modeling work by Brooks et al. (1994) had suggested a similar mechanism, albeit focused on mid- rather than upper-level winds; however, the realism of their simulations was compromised by a lack of ice microphysics. RS98 had planned to undertake their own modeling study, which would form the basis of a follow-up paper; however, the work was never undertaken (E. Rasmussen 2015, personal communication).

Since RS98, the issue of environmental controls on supercell morphology has received very little attention. Beatty et al. (2009) found some support for RS98's hypothesis, with their "rear-reflectivity mode" storms (HPs in the traditional classification) featuring slightly weaker upper-level SR flow than "forward-reflectivity mode" storms (CLs and LPs); however, their sample size was very small (just six storms). More recently, Grant and Van den Heever (2014) found that they could simulate LP-like storms in the absence of strong ULS, simply by introducing dry layers into the idealized thermodynamic sounding of Weisman and Klemp (1982). In agreement with RS98, these storms featured stronger SR flow at upper levels; however, this was associated with changes in storm motion and storm-scale circulation rather than the background shear. The authors' conclusion, that midlevel humidity is a key factor separating CL and LP supercells, is consistent with the tendency for the latter to form close to the Great Plains dryline (Bluestein and Parks 1983).

However, RS98 did not find any significant difference in 0–5-km mean relative humidity between LP and CL environments or, indeed, between LP and HP environments.

Clearly, further work is needed to elucidate fully the environmental factors that influence supercell morphology. To this end, the present study seeks to test the hypothesis of RS98 by simulating supercells across a range of ULS profiles. This also provides an opportunity to investigate more generally the impact of variations in ULS on simulated storms, a question that has thus far been overlooked in the literature on supercell–environment interactions. We begin in section 2 by detailing the numerical experiments performed. Eight primary simulations are conducted, exploring changes in ULS magnitude, vertical distribution, and direction. In addition we consider the sensitivity of our main findings to variations in other environmental parameters that have been shown to influence supercell characteristics. Results from all of these runs are presented in section 3 with a summary and discussion provided in section 4.

2. Methodology

a. Model configuration

Idealized simulations of supercells were performed using the cloud model CM1, release 17 (Bryan and Fritsch 2002; Bryan 2016). The model was configured to solve the compressible governing equations on a three-dimensional domain with rigid, free-slip upper and lower boundaries and open-radiative lateral boundaries. To prevent domain-total mass loss and pressure falls, the restricted outward flux option was enabled, where at the end of each time step the boundary-normal wind components are rescaled to balance the inward and outward mass fluxes. For temporal integration, a Klemp–Wilhelmsen time-splitting scheme (Klemp and Wilhelmsen 1978) was employed with a vertically implicit solver and eight acoustic time steps per full time step. Implicitly diffusive fifth-order advection was used in both the horizontal and vertical with no additional artificial diffusion applied. Subgrid turbulence was parameterized using a turbulent kinetic energy scheme similar to that of Deardorff (1980), while microphysical processes were represented by the double-moment scheme of Morrison et al. (2005) with hail (rather than graupel) as the rimed ice category. Surface fluxes, the Coriolis force, and radiation were all neglected. All of the simulations were run for 3 h and output files were saved every 5 min.

Storms were initiated in a time-invariant horizontally homogeneous environment (detailed below) using a warm bubble centered at an altitude of 1.5 km, with

horizontal and vertical radii of 10 and 1.5 km, respectively, and a maximum potential temperature perturbation of 2 K. The bubble was placed at $(x, y) = (50, 50)$ km in a domain with horizontal dimensions of $240 \text{ km} \times 180 \text{ km}$; these values were chosen to ensure that storms and their associated outflow did not impinge on the lateral boundaries during the simulations. The model top was placed at 20 km with Rayleigh damping applied in the uppermost 4 km to limit spurious reflection of wave energy. A uniform horizontal grid length of $\Delta x = 500 \text{ m}$ was employed, together with a stretched vertical grid, with Δz increasing from 100 m at the surface to 500 m above 12 km (giving a total of 56 levels). It is recognized that horizontal grid lengths of 250 m or less are required to properly capture the turbulent nature of deep convection, in particular the processes of entrainment and detrainment (Bryan et al. 2003; Petch 2006; Lebo and Morrison 2015). To verify that our findings were not strongly influenced by the choice of grid spacing, two sensitivity runs with $\Delta x = 250 \text{ m}$ were performed: one without ULS and one with moderate ULS (SU00 and SU20, described below). Similar tests were also performed using higher vertical resolution and different microphysics schemes. While significant differences were seen in the absolute values of certain quantities (such as updraft area and condensate mass), the changes in storm characteristics associated with increasing shear were found to be consistent with the main findings of this paper.

b. Initial conditions

The initial thermodynamic conditions were specified using the method of McCaul and Weisman (2001). This allows for independent variations of the CAPE, height of maximum buoyancy, mixed-layer depth, relative humidity, and temperature—variables which all uniquely influence supercell characteristics (McCaul and Weisman 2001; McCaul and Cohen 2002; McCaul et al. 2005; James and Markowski 2010; Kirkpatrick et al. 2011). Vertical profiles of potential temperature and mixing ratio are derived based on the first 10 input variables defined in Table 1. Details of the method are given in the appendix. Figure 1 shows the default sounding on a skew T - $\log p$ diagram. Similar to the canonical Weisman and Klemp (1982) sounding, it features a 1-km-deep nearly well-mixed boundary layer, surface-based CAPE (SBCAPE) of 2000 J kg^{-1} , negligible convective inhibition (CIN), a low lifting condensation level (LCL), and relative humidity that decreases steadily from the mixed-layer top (where the air is close to saturation) to the tropopause at 12 km.

The 0–6-km wind profile used in our simulations is the quarter-circle profile of Weisman and Rotunno (2000),

TABLE 1. Parameters used to define the thermodynamic and wind profiles used in our simulations. Default values of variable parameters are indicated with boldface font.

Symbol	Definition (unit)	Value
z_{ml}	Mixed-layer depth (km)	0.5, 1 , 1.5
γ_{ml}	Potential temperature lapse rate in mixed layer ($K \text{ km}^{-1}$)	1
p_{ml}	Pressure at mixed-layer top (hPa)	940, 890 , 840
T_{ml}	Temperature at mixed-layer top (K)	285, 290 , 295
H_{ml}	Relative humidity at mixed-layer top (%)	95
z_{tp}	Tropopause height (km)	12
H_{tp}	Relative humidity at tropopause (%)	25
F	Factor controlling relative humidity decrease	0.5, 1 , 1.5
E	Surface-based CAPE ($J \text{ kg}^{-1}$)	1000, 2000 , 3000
z_B	Height of max buoyancy (km)	6, 7 , 8
z_L	Depth of lower shear layer (km)	6
z_U	Depth of upper shear layer (km)	6
S_L	Lower-layer hodograph length ($m \text{ s}^{-1}$)	25, 30 , 35
S_U	Upper-layer hodograph length ($m \text{ s}^{-1}$)	0, 10, 20, 30
ϕ_U	Change in shear vector orientation across upper layer ($^{\circ}$)	-90, 0, 90

but with a slightly smaller shear magnitude (hodograph length) of 30 m s^{-1} (compared to 35 m s^{-1}). Eight configurations of upper-level (6–12 km) shear were considered. The full profiles for each of these are shown as hodographs in Fig. 2. Each run is given a four-character identifier. The first four simulations (SU00–30) were designed to examine the sensitivity of simulated supercells to variations in ULS magnitude. The shear in these runs is unidirectional and constant over the 6–12-km layer, with the hodograph length varying from 0 to 30 m s^{-1} in 10 m s^{-1} increments (Figs. 2a–d). Using the intermediate ULS magnitude of 20 m s^{-1} , two additional pairs of simulations were then performed. In the first, the vertical distribution of ULS was varied, with shear concentrated in the lower portion of the layer in one simulation (CONL; Fig. 2e) and the upper portion of the layer in the other (CONU; Fig. 2f). In the second, the shear vector was rotated by 90° over the layer, clockwise in one simulation (VEER; Fig. 2g) and counterclockwise in the other (BACK; Fig. 2h). Each wind profile is defined by five variables (Table 1); details of their construction are provided in the appendix.

To explore the impact of variations in ULS across a range of environmental conditions, a total of 14 sensitivity tests were performed using different configurations of CAPE, height of maximum buoyancy, mixed-layer depth, temperature, free-tropospheric humidity, and low-level shear (hodograph length and

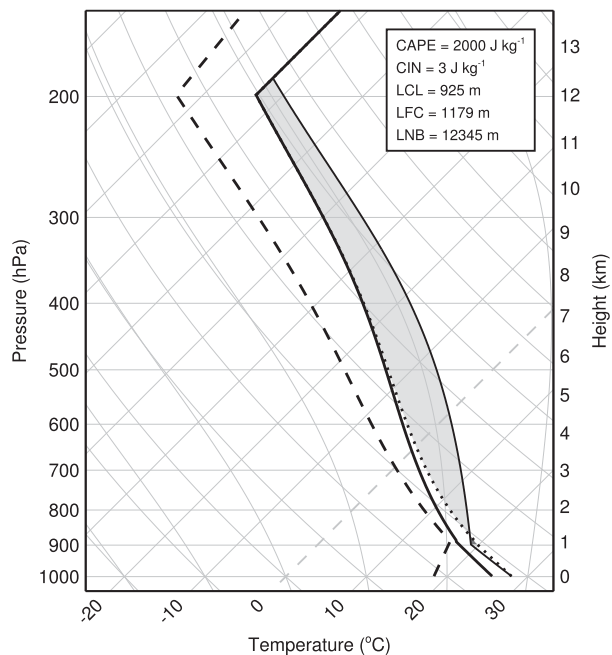


FIG. 1. Skew T -log P diagram showing the default thermodynamic sounding used in our simulations. Thick solid, dashed, and dotted lines show the environmental temperature, dewpoint temperature, and virtual temperature, respectively. The thin solid line shows the virtual temperature of a parcel lifted from the surface, with areas of positive and negative buoyancy above the LCL shaded light and dark gray, respectively (the latter area is very small).

shape). Details are provided in Table 2. In each run only a single parameter was perturbed, apart from in the decreased and increased CAPE runs where the height of the maximum buoyancy, z_B , was also modified. (A decrease in CAPE necessitated a decrease in z_B in order to prevent the rapid decay of storms, while an increase in CAPE necessitated an increase in z_B to prevent the low-level lapse rate from becoming superadiabatic.) To reduce computational and storage requirements, all of these experiments were only performed for the SU00 and SU20 configurations of ULS.

To verify the realism of our environmental conditions, values of key parameters were compared against those derived from the proximity sounding dataset of Thompson et al. (2007). These soundings were obtained from hourly Rapid Update Cycle (RUC) model analyses in the vicinity of 835 supercells observed over the contiguous United States during 1999–2005. A total of 70 profiles, featuring SBCAPE of less than 100 J kg^{-1} , were considered unrepresentative and excluded from our analysis. The results of this comparison, shown in Fig. 3, indicate that the parameters used in this study all fall within their observed range. Critically, the range of values considered here for ULS

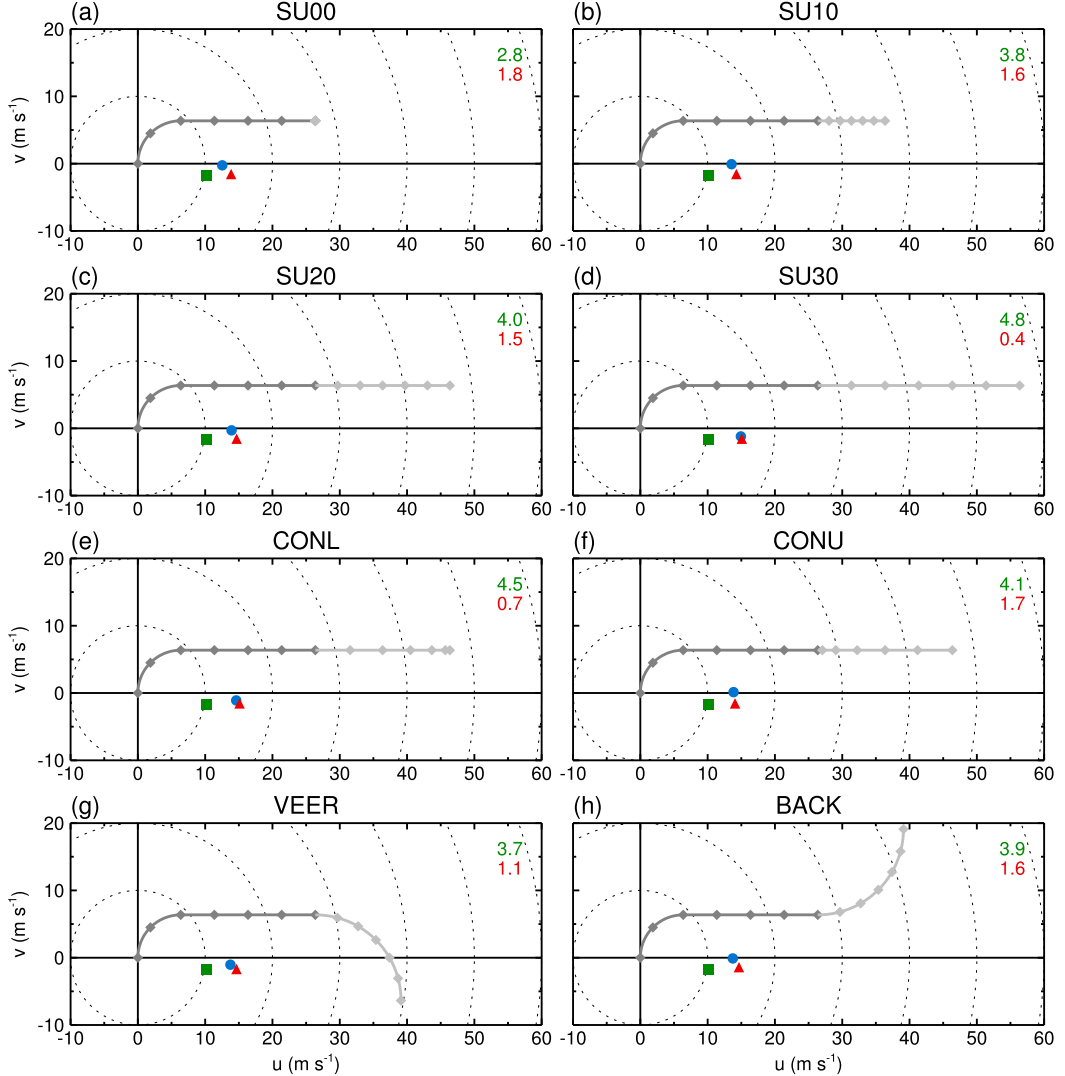


FIG. 2. Hodographs showing the eight configurations of ULS used in our simulations. The 0–6- and 6–12-km wind profiles are plotted in dark and light gray, respectively, with height markers (diamonds) every 1 km. Blue circles show the simulated storm motion for $t = 1\text{--}3\text{ h}$, while green squares and red triangles show predictions obtained using the original (0–6-km mean wind) and modified (0–8-km mean wind) Bunkers et al. (2000) method, respectively (the former prediction is identical in every case). The magnitude of the vector error associated with each prediction is given in the top-right corner of each panel.

(quantified by the 6–12-km bulk wind difference; Fig. 3h) spans over 95% of the observed distribution (without producing unrealistically high anvil-level winds; Fig. 3i).

It must be noted, however, that our soundings are considerably moister than the majority of those characterizing supercell environments in the United States, particularly in the bottom half of the troposphere (Fig. 3d). In fact, the low-level humidity of the driest sounding we consider (FH05; Table 2) is still around 10% higher than the largest value in RS98's sample of proximity soundings from the Great Plains (cf. their

Fig. 5). It was found that storms could not be sustained in simulations with drier profiles (lower values of the parameter F ; Table 1), which is typical when using a warm bubble to initialize convection, at least in horizontally homogeneous environments (McCauley and Cohen 2004; Bunkers 2010; Naylor and Gilmore 2012). This difference between simulated and observed storm environments may limit the relevance of our findings to the hypothesis of RS98, a possibility that is discussed further in section 4. Nevertheless, Fig. 3 suggests that our results should, at the very least, be relevant to real supercells in moist environments. Investigation of the

TABLE 2. Details of simulations used to investigate the sensitivity of our results to variations in environmental parameters. Each of these was performed twice, with the SU00 and SU20 configurations of ULS.

Identifier	Description
SL25	Decreased low-level shear ($S_L = 25 \text{ m s}^{-1}$)
SL35	Increased low-level shear ($S_L = 35 \text{ m s}^{-1}$)
ZB06	Decreased height of max buoyancy ($z_B = 6 \text{ km}$)
ZB08	Increased height of max buoyancy ($z_B = 8 \text{ km}$)
C1Z6	Decreased CAPE ($E = 1000 \text{ J kg}^{-1}$, $z_B = 6 \text{ km}$)
C3Z8	Increased CAPE ($E = 3000 \text{ J kg}^{-1}$, $z_B = 8 \text{ km}$)
T285	Decreased temp ($T_{ml} = 285 \text{ K}$)
T295	Increased temp ($T_{ml} = 295 \text{ K}$)
ML05	Decreased mixed-layer depth ($z_{ml} = 500 \text{ m}$)
ML15	Increased mixed-layer depth ($z_{ml} = 1.5 \text{ km}$)
FH05	Decreased humidity above the mixed layer ($F = 0.5$)
FH15	Increased humidity above the mixed layer ($F = 1.5$)
HSTR	Straight 0–6-km hodograph
HSEM	Semicircular 0–6-km hodograph

role of ULS in drier environments, using a more sophisticated method of convection initiation (e.g., Loftus et al. 2008; Naylor and Gilmore 2012), is deferred to future work.

3. Results

In all simulations, the initial warm bubble triggers an isolated convective cell that splits during the first hour into left- and right-moving storms. As a result of the clockwise turning of the low-level shear vector, the latter becomes the dominant supercell while the former develops more multicellular characteristics (not shown). Our analysis focuses exclusively on the right-moving storm during the final 2 h of the simulations. To this end, the storm is tracked and its characteristics analyzed using moving windows centered on its location at each output time. Specifically, we track the midlevel updraft core, defined here as a contiguous region with 3–6-km mean vertical velocities above a threshold. To account for temporal variations in updraft intensity, a percentile-based threshold is used; namely, the 95th percentile of velocities above 1 m s^{-1} . Following Lakshmanan et al. (2015), the u and v components of storm motion are estimated by applying a Theil-Sen fit to the storm centroid coordinates as a function of time. This calculation is performed three times for each simulation: once for

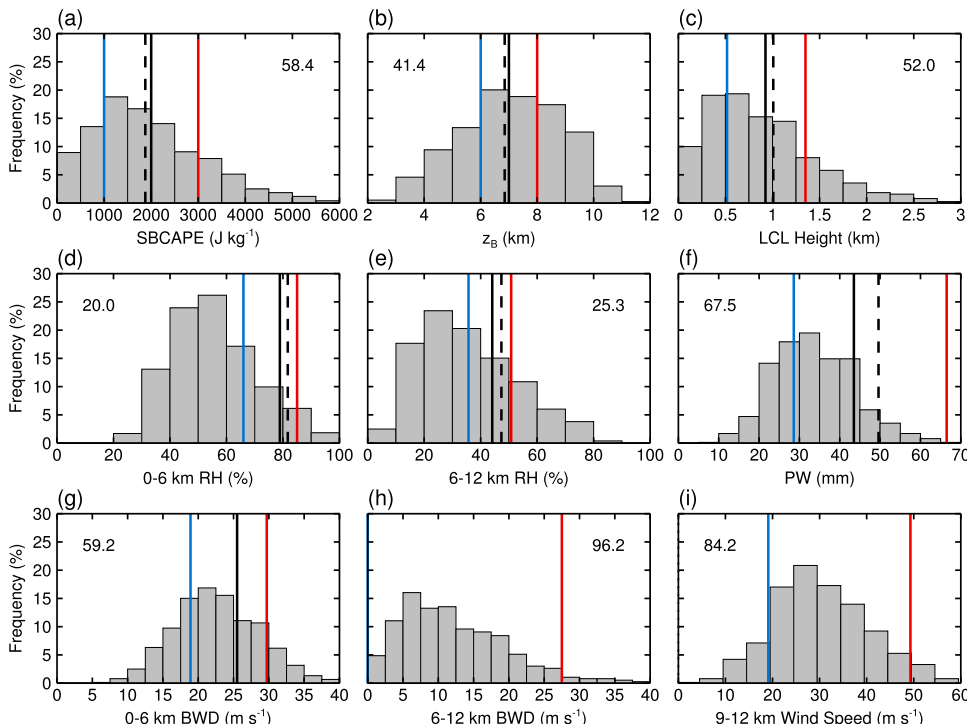


FIG. 3. Histograms showing the probability density function for nine parameters derived from the supercell proximity sounding dataset of Thompson et al. (2007): (a) SBCAPE; (b) height of maximum buoyancy z_B ; (c) LCL; (d) 0–6-km mean relative humidity (RH); (e) 6–12-km mean RH; (f) precipitable water (PW); (g) 0–6 km bulk wind difference (BWD); (h) 6–12-km BWD; and (i) 9–12-km mean wind speed. Note that BWD was computed using wind components averaged over 500 m at either end of the layer (e.g., 0–500 and 5500–6000 m for the 0–6-km BWD). Solid black, blue, and red vertical lines show, respectively, the default, minimum, and maximum values considered in our simulations. Since there is no default setting for upper-level winds, black lines are not included in (h) and (i). The blue line in (h) is at $x = 0$ and is thus obscured by the y axis. Dashed black vertical lines in (a)–(f) show values for the canonical Weisman and Klemp (1982) sounding (with a surface mixing ratio of 14 g kg^{-1}). Numbers in each panel give the percentage of observed values that fall within the simulated range.

TABLE 3. Summary diagnostics for all simulations with variations in ULS. SRH is storm-relative helicity and the symbols R and U denote rainfall accumulation and surface wind speed, respectively. For SU10, SU20, and SU30, numbers in parentheses give the percentage change compared to SU00; for CONL, CONU, VEER, and BACK, they give the percentage change compared to SU20.

	SU00	SU10	SU20	SU30	CONL	CONU	VEER	BACK
Storm speed (m s^{-1})	12.5	13.6 (+9)	13.9 (+11)	15.0 (+20)	14.7 (+6)	13.9 (0)	13.8 (-1)	13.7 (-1)
Storm direction ($^{\circ}$)	91.1	90.3 (-1)	91.2 (0)	94.6 (4)	94.3 (3)	89.5 (-2)	94.3 (+3)	90.5 (-1)
0–3-km SRH ($\text{m}^2 \text{s}^{-2}$)	137.6	142.1 (+3)	147.0 (+7)	163.7 (+19)	160.5 (+9)	141.6 (-4)	154.3 (+5)	143.7 (-2)
9-km U_{sr} (m s^{-1})	15.3	18.9 (+24)	23.4 (+53)	27.5 (+80)	27.0 (+15)	19.4 (-17)	21.9 (-6)	23.9 (+2)
Track length (km)	90.3	98.3 (+9)	101.7 (+13)	108.0 (+20)	106.5 (+5)	103.6 (+2)	100.5 (-1)	97.5 (-4)
R_{max} (mm)	35.7	36.7 (+3)	44.2 (+24)	47.2 (+32)	46.0 (+4)	51.1 (+16)	39.4 (-11)	41.6 (-6)
$R \geq 25 \text{ mm}$ swath width (km)	2.5	4.0 (+60)	5.7 (+128)	6.3 (+152)	6.3 (+11)	4.4 (-23)	5.6 (-2)	5.5 (-4)
U_{max} (m s^{-1})	38.4	40.3 (+5)	44.2 (+15)	43.5 (+13)	47.9 (+8)	39.8 (-10)	43.2 (-2)	44.5 (-1)
$U \geq 26 \text{ m s}^{-1}$ swath width (km)	3.5	10.4 (+197)	15.8 (+351)	13.1 (+274)	19.2 (+22)	12.6 (-20)	13.5 (-15)	18.1 (+15)

the full final 2 h ($t = 1\text{--}3 \text{ h}$) and separately for $t = 1\text{--}2$ and $2\text{--}3 \text{ h}$.

Analysis of the 36 simulations is divided into three sections. In the first, we consider those runs where the magnitude of ULS was varied (SU00, SU10, SU20, and SU30), while the second deals with cases of nonuniform and directionally varying shear (CONL, CONU, VEER, and BACK). In the final section, we explore the sensitivity of our findings to variations in other environmental parameters. Summary diagnostics for the first two sets of runs, computed over the final 2 h of simulation time are given in Table 3. Storm severity is quantified by the maximum values and “swath widths” of accumulated rainfall, R , and surface wind speed, U . Swath widths are computed by applying a minimum threshold to each quantity ($R = 25 \text{ mm}$, $U = 26 \text{ m s}^{-1}$; the former is arbitrary while the latter corresponds to the Storm Prediction Center’s definition of severe winds), computing the area impacted by that hazard (within the portion of the domain containing the right-moving storm), and normalizing by the track length.

a. Variations in upper-level shear magnitude

We first note that as ULS increases in magnitude from 0 to 30 m s^{-1} , the simulated storm speed also increases (Table 3). This suggests that supercell motion is not solely governed by the 0–6-km winds, a result that stands in contrast to the majority of observationally based methods developed to predict it (Davies and Johns 1993; Davies 1998; Rasmussen and Blanchard 1998; Bunkers et al. 2000). An exception is Ramsay and Doswell

(2005), who found that the accuracy of the widely used Bunkers et al. (2000) method could be improved by using the 0–8-km (rather than 0–6 km) mean wind in the calculation. Their assertion is supported by our results: estimates of storm motion obtained using the modified algorithm have consistently smaller errors (Fig. 2). However, more recent observational studies, utilizing larger datasets, have agreed with Bunkers et al. (2000), finding 0–6 km to be the optimal mean-wind layer (Thompson et al. 2007; Bunkers et al. 2014). This discord may be related to our idealized shear profiles, but could also reflect a systematic model bias, a possibility we return to in section 4.

The increase in storm motion with increasing ULS may simply be a consequence of enhanced advection due to the stronger upper-level flow. However, mature supercells also move through continuous propagation associated with dynamic VPPGAs and discrete new updraft development along the leading edge of their outflow (Zeitler and Bunkers 2005). It is likely that the changes in storm characteristics detailed below act to enhance these forcing mechanisms, driving a feedback on the storm motion in the latter portion of the simulations. Evidence for such a feedback is provided in Table 4, which shows that acceleration of the storm between the second and third hours of the simulation generally increases with increasing ULS.

It should be noted that despite the increase in storm motion, there is still a pronounced increase in upper-level SR flow with increasing ULS. At 9 km, the SR wind speed increases from 15.3 m s^{-1} in SU00 to 27.5 m s^{-1} in

TABLE 4. Comparison of calculated storm speeds U_s for $t = 1$ –2 and 2–3 h, and the difference between the two, ΔU_s , for the SU00, SU10, SU20, and SU30 runs.

Run	U_s (m s^{-1})	ΔU_s (m s^{-1})
	1–2 h	1–3 h
SU00	12.1	12.8
SU10	12.6	14.4
SU20	12.7	15.6
SU30	13.8	16.0
		2.2

SU30 (Table 3). These values approximately span the 18 – 28 m s^{-1} range over which RS98 observed a transition in supercell morphology from predominantly HP to predominantly LP. We might thus expect a similar transition to occur across our four simulations.

Figure 4 summarizes the evolution of the SU00–30 runs through two diagnostics computed over the full 3-h simulation time: the 5-km updraft “swath” (maximum vertical velocity at 5 km, computed at every horizontal grid point across all model time steps) and the accumulated surface rainfall. The updraft intensity appears to be quite consistent among the first three runs; however, in SU30 it is noticeably reduced between $t = 90$ and 155 min. Further analysis suggests that this weakening is associated with

surging rear-flank outflow, which temporarily disrupts the supply of potentially buoyant air at low levels (not shown). Similar behavior in SU20 is responsible for the brief weakening of the updraft around $t = 90$ min. It thus appears that there is a tendency toward outflow dominance as ULS is increased from 0 to 30 m s^{-1} . This tendency is explained by a dramatic increase in rainfall intensity (right column in Fig. 4; Table 3), which, through enhanced evaporative cooling, promotes lower cold-pool temperatures and stronger outflow winds (Table 3). These are surprising results; based on the observations of RS98, we would expect a decrease in precipitation and outflow intensity with increasing ULS.

Figures 5 and 6 illustrate the changes in storm structure that accompany variations in ULS magnitude. Both show composite fields produced by averaging the 5-min output over the second and third hours of the simulation using domains that follow the tracked midlevel updraft. This averaging allows for a fairer comparison between the runs as it smoothes out short-time-scale fluctuations in storm structure and intensity, which can mask systematic differences at a particular time step.

The increase in rainfall and outflow intensity with increasing shear is clearly seen in Fig. 5, as is the associated reduction in cold-pool temperatures (shown by

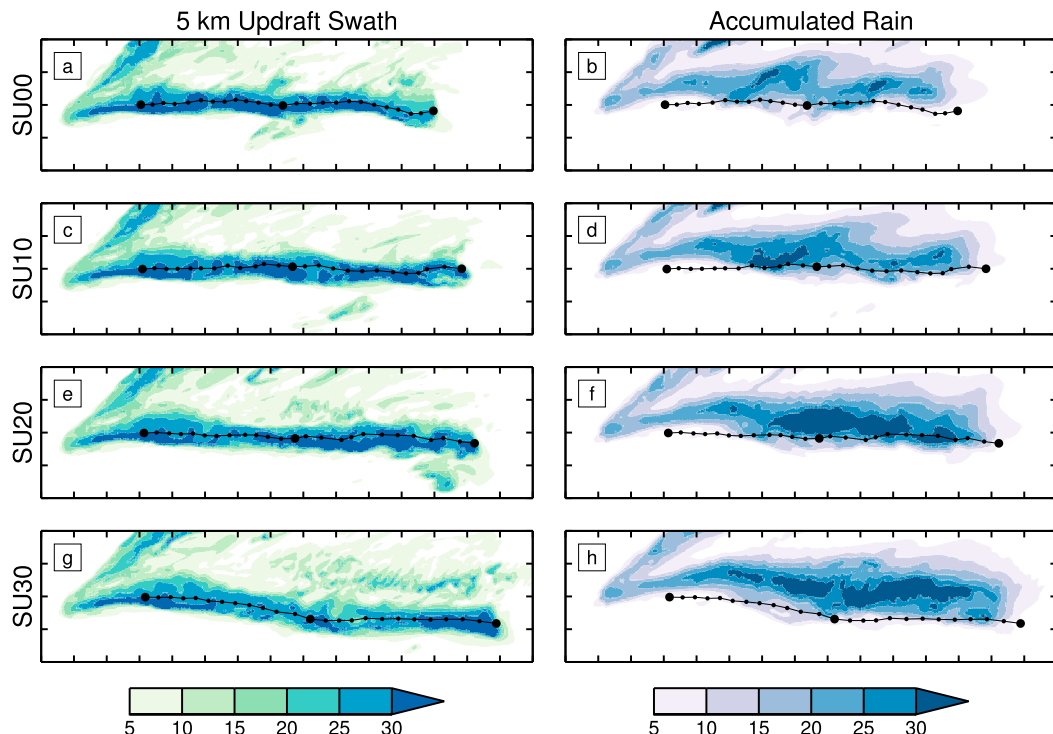


FIG. 4. (left) Swath of 5-km updraft velocity (m s^{-1}) and (right) accumulated rainfall (mm) for (top to bottom) the SU00, SU10, SU20, and SU30 runs. The storm track for $t = 1$ –3 h is shown in each panel with small and large circles marking 5- and 60-min intervals, respectively. The domain shown extends from $x = 50$ to 200 km and $y = 40$ to 80 km, with tick marks on the axes spaced at 10-km intervals.

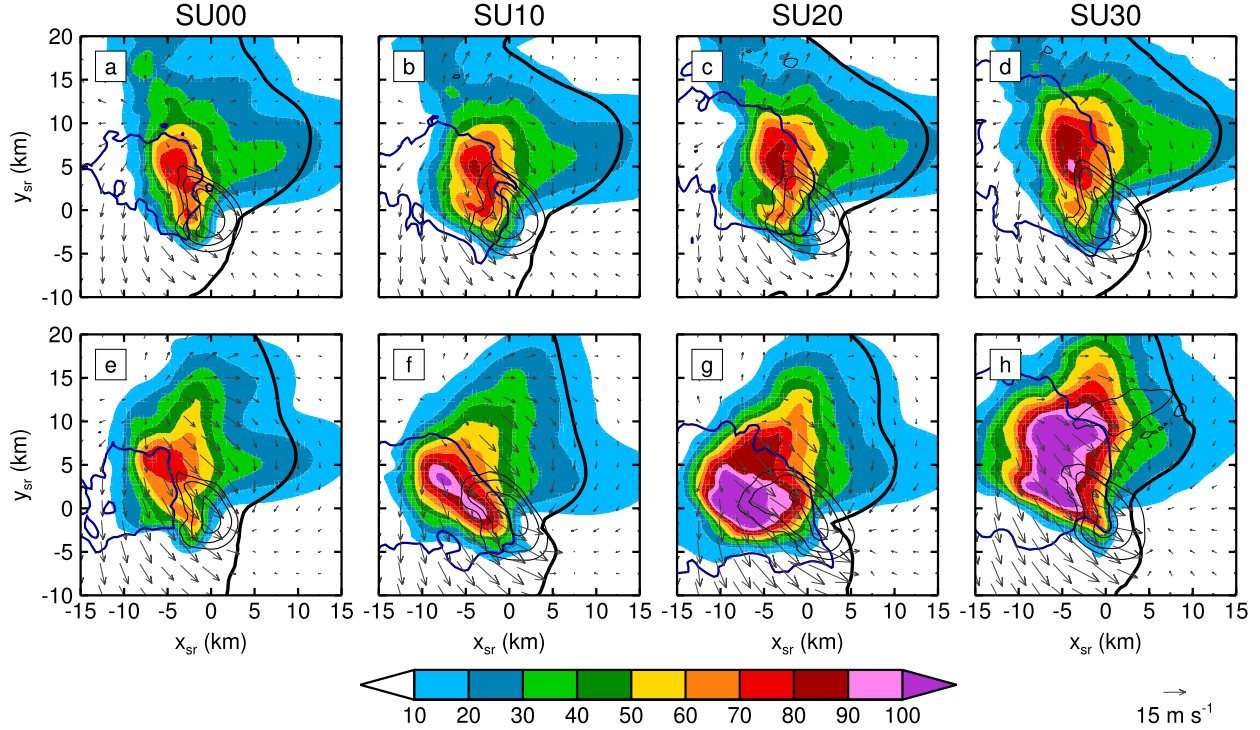


FIG. 5. Composites plan views for (left to right) the SU00, SU10, SU20, and SU30 runs, computed over (a)–(d) $t = 1\text{--}2$ and (e)–(h) $t = 2\text{--}3$ h. Variables shown are surface rain rate (colors; mm h^{-1}), 3–6-km average vertical velocity (thin black contours; 5, 10, and 20 m s^{-1}), cold-pool boundary (thick black contour; $\theta' = -1 \text{ K}$ at $z = 50 \text{ m}$), $\theta' = -5 \text{ K}$ at $z = 50 \text{ m}$ (blue contour), and ground-relative winds at $z = 50 \text{ m}$ (vectors, plotted every 2.5 km; reference vector in bottom right).

the areal expansion of the -5-K perturbation-potential-temperature contour). These differences are slight for $t = 1\text{--}2$ h, but substantial for $t = 2\text{--}3$ h. Overall, the simulated storm tends toward a more HP-like structure with increasing ULS, with heavy precipitation concentrated in the rear flank of the storm, which is precisely the opposite of what RS98 hypothesized. We also note an increase in updraft area with increasing ULS, although in the final hour the trend is reversed between SU20 and SU30 because of the aforementioned temporary weakening of the storm in the latter simulation. At this time, a secondary area of ascent can be seen to the north of the main updraft in SU30 (Fig. 5h). This feature is associated with the development of multiple small updrafts (visible in Fig. 4g) along the storm's forward-flank gust front. It appears that the strong outflow in this run ultimately promotes a storm mode that lies between the HP-supercell and multicell archetypes. Similar "hybrid" storms (e.g., Nelson 1987) have been simulated in other environments that favor outflow dominance, such as those with a high LCL (McCaull and Cohen 2002).

The composite cross sections in Fig. 6 reveal the presence of a more tilted updraft in the runs with ULS, with enhanced downshear advection of condensate at upper levels. In SU00, the storm quickly develops a

back-sheared anvil as strong divergence around the tropopause overwhelms the background westerly flow (Fig. 6a). For $t = 1\text{--}2$ h, this feature is less pronounced in SU10 (Fig. 6b) and completely absent in SU20 and SU30 (Figs. 6c,d). Over time, all four storms become more upright as the upper-level flow is decelerated and deflected by the updraft. A back-sheared anvil ultimately develops in SU10 and SU20 (Figs. 6f,g) but is still absent in the SU30 composite for $t = 2\text{--}3$ h (Fig. 6h). This may be explained by the combination of even stronger upper-level SR winds and a narrower updraft (with associated weaker cloud-top divergence) compared to the other runs. Figure 6 also shows an increase in both the maximum and area-averaged total condensate mixing ratio with increasing ULS, at least up to SU20.

Further insight into the vertical structure of the storms is provided in Figs. 7 and 8, which show composite vertical profiles computed over a $20 \times 20 \text{ km}^2$ domain centered on the midlevel updraft centroid at each output time. Figure 7 shows the area-integrated mass flux (mass flow rate), area, average velocity, and average effective buoyancy (defined below) of the primary updraft, defined as the largest contiguous volume where $w \geq 5 \text{ m s}^{-1}$. Figure 8 shows the mass of each of the model's five liquid and ice water species: cloud water,

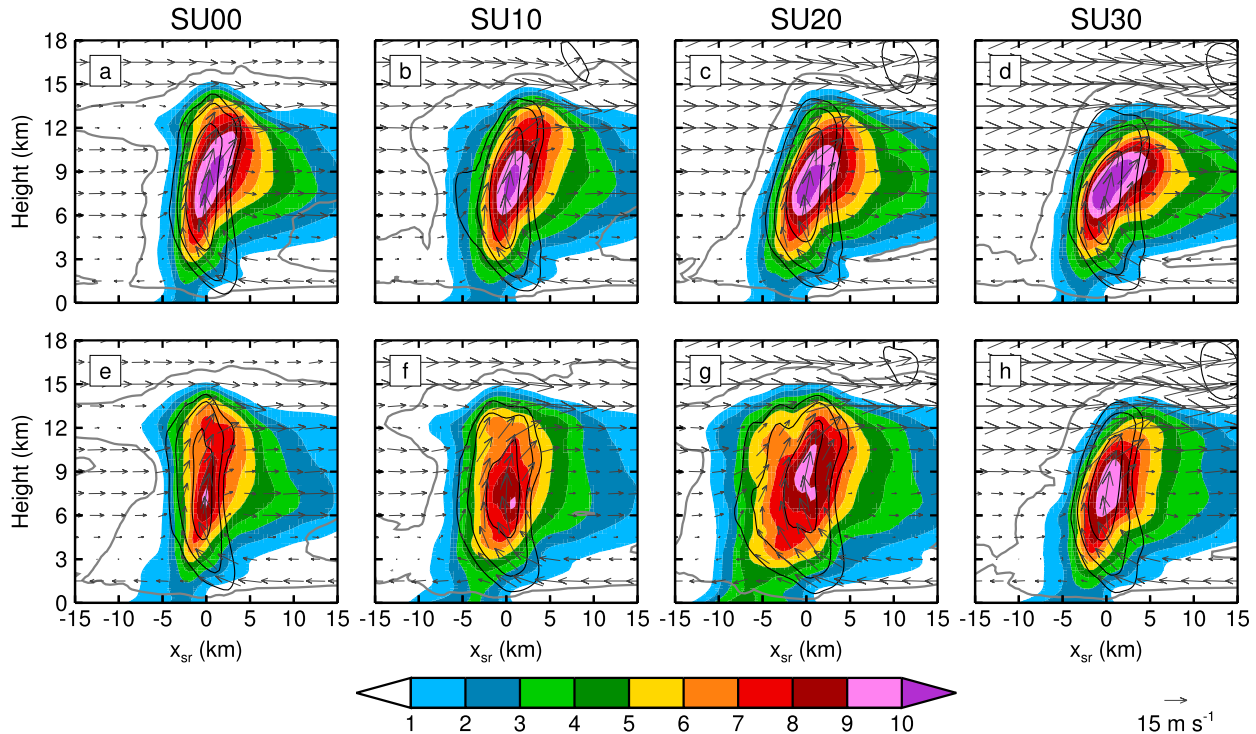


FIG. 6. Composite vertical cross sections for (left to right) SU00, SU10, SU20, and SU30 runs, computed over (a)–(d) $t = 1\text{--}2$ and (e)–(h) $t = 2\text{--}3$ h. Variables shown are total condensate mixing ratio (colors; g kg^{-1}), vertical velocity (thin black contours; 5, 10, and 20 m s^{-1}), cloud boundary (gray contour; $q_c + q_i = 0.01 \text{ g kg}^{-1}$), and storm-relative winds (vectors, plotted every 2.5 km in the horizontal and 1.5 km in the vertical). Cross sections are taken from west to east at $y_{sr} = 0$ with values averaged over a width of 5 km.

cloud ice, rain, snow, and hail. Interpretation of changes in condensate mass is aided by Fig. 9, which shows, for each species, the contribution from all other water species (including water vapor) to increases in their mass, computed over the same $20 \times 20 \text{ km}^2$ moving domain.

Initially, there is a slight increase in updraft mass flux with increasing ULS at midlevels, but a decrease in the upper portion of the storm in the stronger shear cases (Fig. 7a). During the final hour, the mass flow rate in SU20 is approximately double that in SU00 at all levels, with SU10 falling almost exactly between the two (Fig. 7e). In SU30, intermediate mass flow rates are obtained at midlevels, but the values are smaller even than those in SU00 above the tropopause. These differences are associated with the previously noted changes in updraft area (Figs. 7b,f). The mean updraft velocity meanwhile generally decreases with increasing ULS, especially above 6 km (Figs. 7c,g). This trend can be explained by considering the vertical profile of effective buoyancy:

$$\beta = B - \frac{1}{\bar{\rho}} \frac{\partial p'_b}{\partial z}, \quad (1)$$

where B is the thermal buoyancy, $\bar{\rho}$ is the base-state density, and p'_b is the buoyancy perturbation pressure.

The second term on the right-hand side of (1) represents the component of the VPPGA due to buoyancy (Davies-Jones 2003; Doswell and Markowski 2004). The effective buoyancy shows a pronounced decrease with increasing ULS between about 2 and 10 km (Figs. 7d,h), indicating a reduction in the energy available to rising air parcels. Further analysis reveals that this decrease is primarily due to an increase in the p'_b term (not shown), which is to be expected given the increase in updraft width and tilt (Parker 2010; Morrison et al. 2016a,b; Jeevanjee and Romps 2016).

Turning to Fig. 8, we note a large, monotonic increase in cloud water mass with increasing shear for $t = 1\text{--}2$ h (Fig. 8a), associated with the increase in updraft area (a larger region of adiabatic cooling and condensation). The opposite trend is observed for cloud ice, reflecting both the reduced mass flux at upper levels and enhanced advection of this species away from the updraft (and out of the $20 \times 20 \text{ km}^2$ box) under stronger SR flow. The same processes contribute to a reduction in snow and hail mass at upper levels (Figs. 8c,d). Meanwhile, rain mass is increased in the presence of ULS (Fig. 8b), primarily as a result of enhanced accretion of cloud water within the larger updrafts (Fig. 9a). In the final hour of the simulations ($t = 2\text{--}3$ h), the trend for cloud water persists

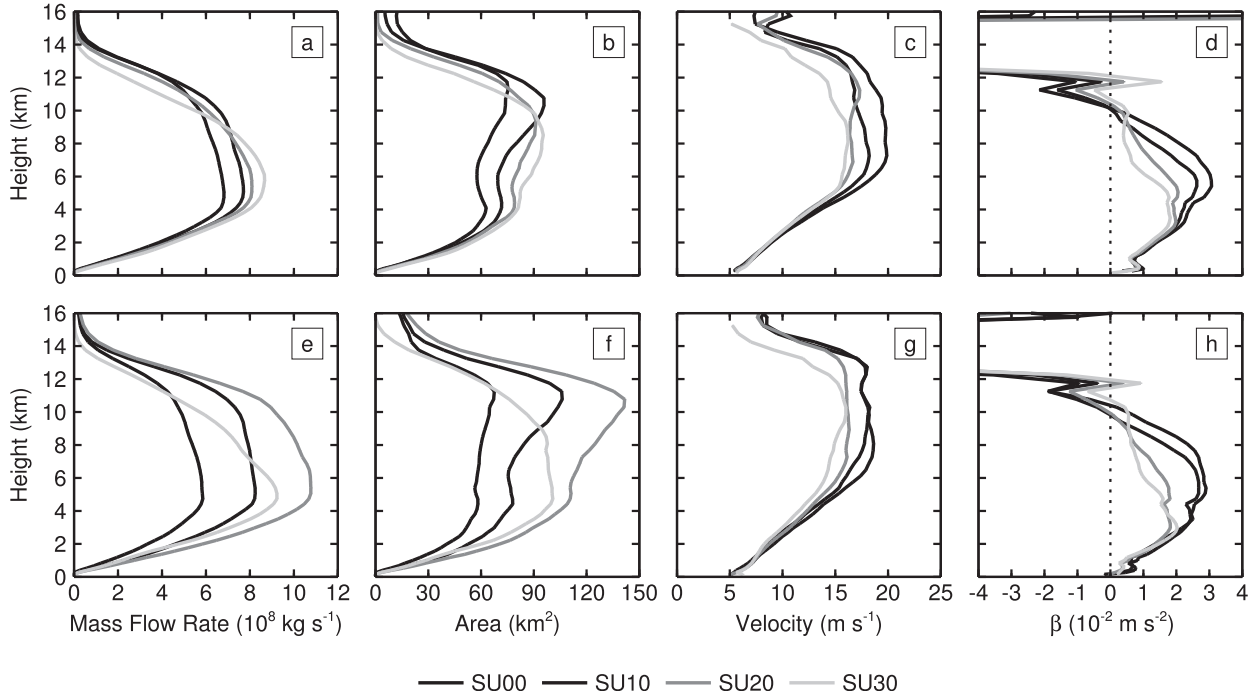


FIG. 7. Composite vertical profiles for the SU00, SU10, SU20, and SU30 runs, computed over (a)–(d) $t = 1\text{--}2$ and (e)–(h) $t = 2\text{--}3$ h. Variables shown are (left to right) updraft-total mass flow rate, updraft area, updraft-average vertical velocity, and updraft-average effective buoyancy. The updraft is defined as the largest contiguous volume with $w \geq 5 \text{ m s}^{-1}$ within a $20 \times 20 \text{ km}^2$ moving domain centered on the midlevel updraft centroid.

(consistent with the trend in updraft area), but the cloud ice mass in SU10 and SU20 recovers to about the same magnitude as in SU00 (Fig. 8e). This recovery is associated with the aforementioned development of a back-sheared anvil in these runs. In contrast, the cloud ice mass remains significantly lower for the persistently downshear-tilted SU30 storm. Snow and hail mass now show a pronounced increase, with ULS up to 20 m s^{-1} (Figs. 8g,h), reflecting enhanced growth of these species through deposition and collection processes within the larger updraft (Fig. 9b). Rain mass also increases across these runs (Fig. 8f), again via enhanced accretion, but also via the melting of a larger mass of hail (Fig. 9b). In SU30, intermediate mass values are found for rain and, below 9 km, snow and hail because of the similarly intermediate updraft area (Fig. 7f) and associated differences in hydrometeor growth (Fig. 9b); however, at higher levels the snow and hail mass remain smaller than in SU00.

The foregoing analysis suggests that the increase in precipitation intensity as ULS is increased from 0 to 20 m s^{-1} results from an increase in updraft area that promotes enhanced cloud water production and hydrometeor growth. The increase in updraft area appears to originate in the lowest few kilometers of the storm, in association with enhanced inflow and convergence on the leading (eastern) edge of updraft (Fig. 10). For $t = 1\text{--}2$ h,

the low-level SR flow in this region increases monotonically with increasing shear (by about 2 m s^{-1} between SU00 and SU30). Later, we observe a more substantial increase for ULS of $0\text{--}20 \text{ m s}^{-1}$ but a decrease as the shear is increased further to 30 m s^{-1} . The changes in SR flow also appear to contribute to variations in updraft shape and orientation during the final simulation hour (e.g., the elongated, southeast-to-northwest-orientated updraft in SU20) via similar variations in the regions of low-level convergence.

To what extent are these changes in SR flow due to the previously noted increase in storm motion with ULS versus perturbations to the low-level background flow? This question is addressed in Fig. 11, which shows composite hodographs of the $0\text{--}3$ -km winds averaged over a $5 \times 5 \text{ km}^2$ area immediately northeast of the updraft (shown in Fig. 10) for $t = 1\text{--}2$ and $2\text{--}3$ h. It is apparent that the flow in this region is strongly perturbed, with northwesterly winds at the surface (associated with the storms' outflow; Fig. 5) veering to south-southeasterly at 3 km (approximately the top of the inflow layer; Fig. 6). For $t = 1\text{--}2$ h, the wind profiles for each run are very similar, indicating that the slight increase in SR flow with ULS during this time is largely due to the enhanced storm motion (Table 4). However, for $t = 2\text{--}3$ h, the winds in SU10 and SU20 have an enhanced easterly component at

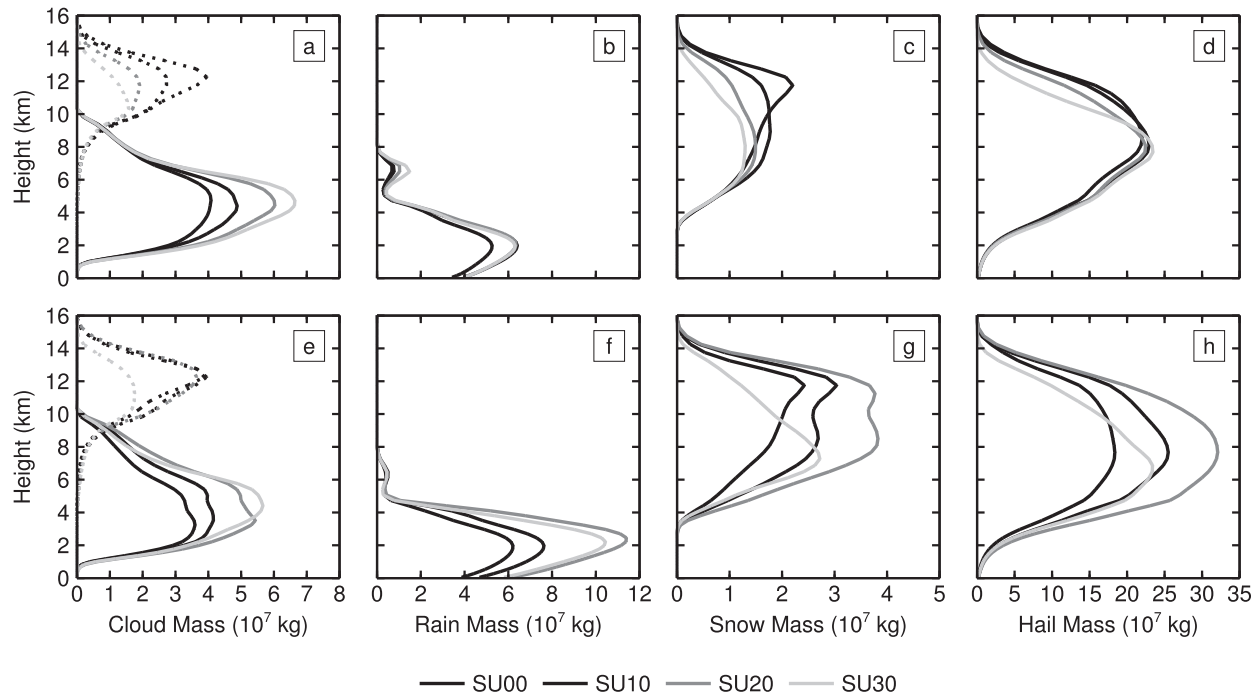


FIG. 8. As in Fig. 7, but for cloud water and cloud ice mass (solid and dotted lines, respectively), rain mass, snow mass, and hail mass.

all levels compared to SU00, while the opposite is true for SU30. Thus, in the final hour of the simulations, changes in both storm motion and the ambient wind contribute to the observed trends in SR flow with increasing ULS.

The easterly low-level perturbation flow to the northeast of the supercell updraft forms in response to negative pressure perturbations in this region (Fig. 12). These are initially of a similar magnitude across the simulations, but become larger in SU10 and SU20 and

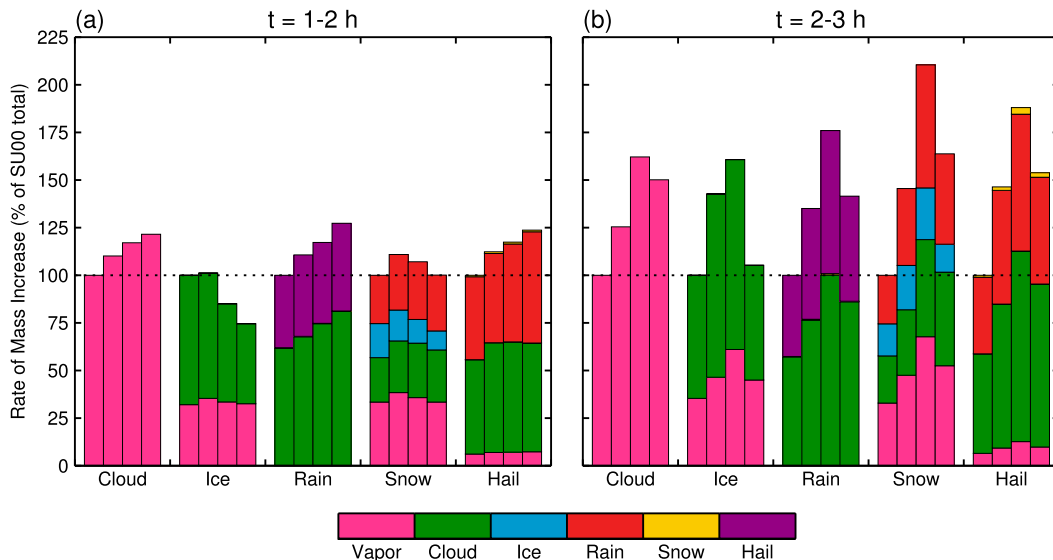


FIG. 9. Stacked bar chart showing the time-averaged contribution of each of the model's six water species to the rate of increase in mass of cloud water, cloud ice, rain, snow, and hail for (a) $t = 1-2$ and (b) $t = 2-3$ h. The bars for each variable show values for (left to right) the SU00, SU10, SU20, and SU30 runs, each scaled by the total rate of increase in mass for SU00. Values were computed over a 20×20 km 2 moving domain centered on the midlevel updraft centroid.

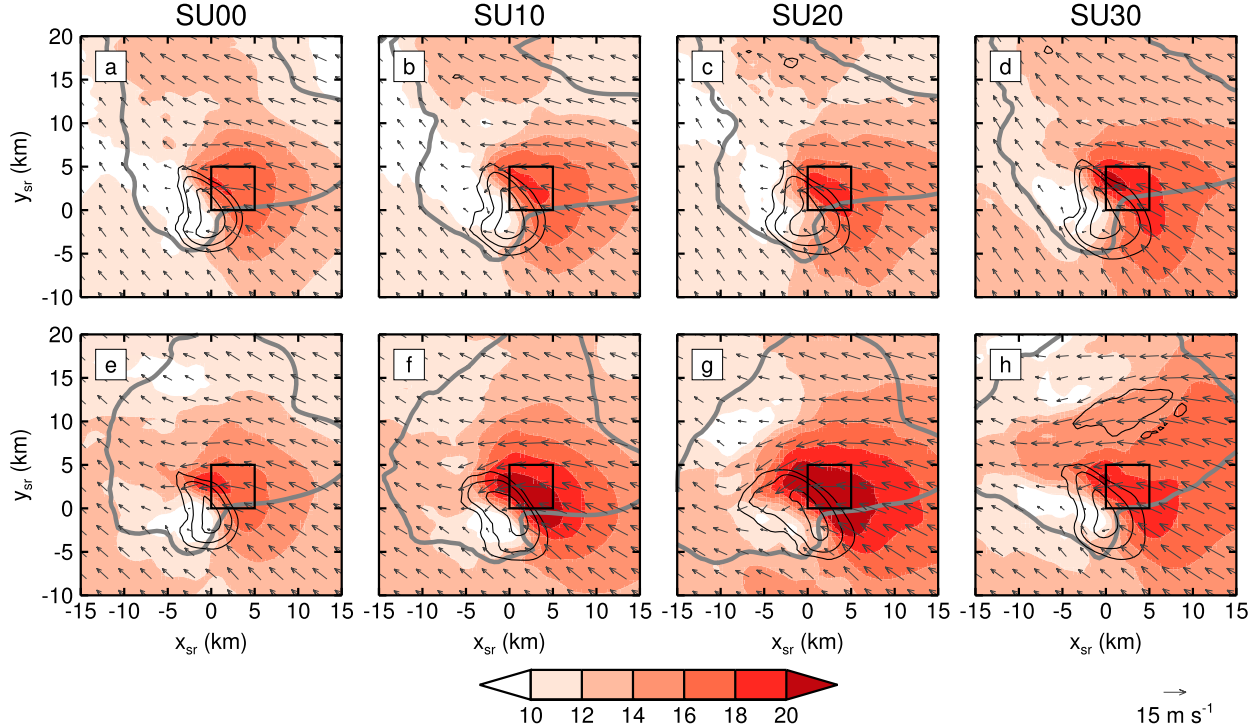


FIG. 10. Composite plan views for (left to right) the SU00, SU10, SU20, and SU30 runs, computed over (a)–(d) $t = 1\text{--}2$ and (e)–(h) $t = 2\text{--}3$ h. Variables shown are 0–3 km-average storm-relative wind speed (colors; m s^{-1}), 3–6 km-average vertical velocity (thin black contours; 5, 10, and 20 m s^{-1}), 10 mm h^{-1} surface rain-rate outline (thick gray contour), and 0–3 km-average storm-relative winds (vectors, plotted every 2.5 km; reference vector in bottom right). Black box shows the area used to compute the hodographs in Fig. 11.

smaller in SU30 compared to SU00 during the final hour. To explore the reason for these differences, the perturbation pressure, p' , was decomposed into buoyancy, linear-dynamic, and nonlinear-dynamic components (p'_b , p'_{dl} , and p'_{dn} , respectively). Physical interpretation of these components is aided by the following expressions, which are valid for well-behaved, incompressible, storm-scale flows (Markowski and Richardson 2010, p. 30):

$$p'_b \propto \frac{\partial B}{\partial z}, \quad (2a)$$

$$p'_{\text{dl}} \propto 2\bar{\mathbf{S}} \cdot \nabla_h w', \quad \text{and} \quad (2b)$$

$$p'_{\text{dn}} \propto e_{ij}^2 - \frac{1}{2}|\boldsymbol{\omega}'|^2. \quad (2c)$$

Here, e_{ij} are the components of the deformation tensor, $\boldsymbol{\omega}$ is the three-dimensional vorticity vector, and $\bar{\mathbf{S}}$ is the two-dimensional vertical shear vector. Overbars indicate the horizontally homogeneous base state and primes indicate perturbations from this base state. The nonlinear-dynamic perturbation pressure is associated with two effects: flow deformation (the “splat” term), which promotes positive p'_{dn} , and rotation (the “spin” term), which promotes negative p'_{dn} . The linear-dynamic perturbation pressure is associated with the

“updraft in shear” effect, which promotes positive and negative p'_{dl} , respectively, on the upshear and downshear sides of an updraft. The buoyancy perturbation pressure is associated with vertical gradients in the thermal buoyancy and tends to be negative where B increases with height and positive where B decreases with height.

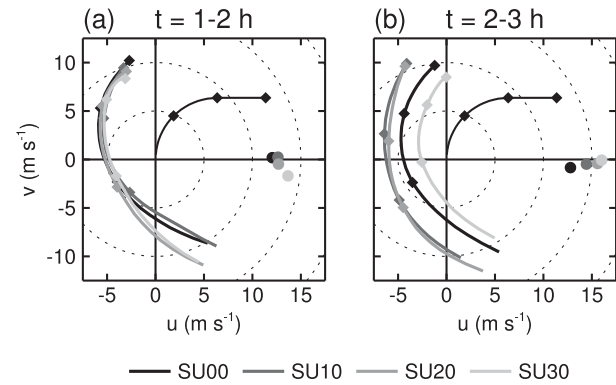


FIG. 11. Composite hodographs showing 0–3-km ground-relative winds (lines) and storm motion (circles) for the SU00, SU10, SU20, and SU30 runs, computed over (a) $t = 1\text{--}2$ and (b) $t = 2\text{--}3$ h. The thin black line shows the background 0–3-km wind profile. Diamonds indicate heights of 1, 2, and 3 km. Winds were averaged over the $5 \times 5 \text{ km}^2$ box shown in Fig. 10.

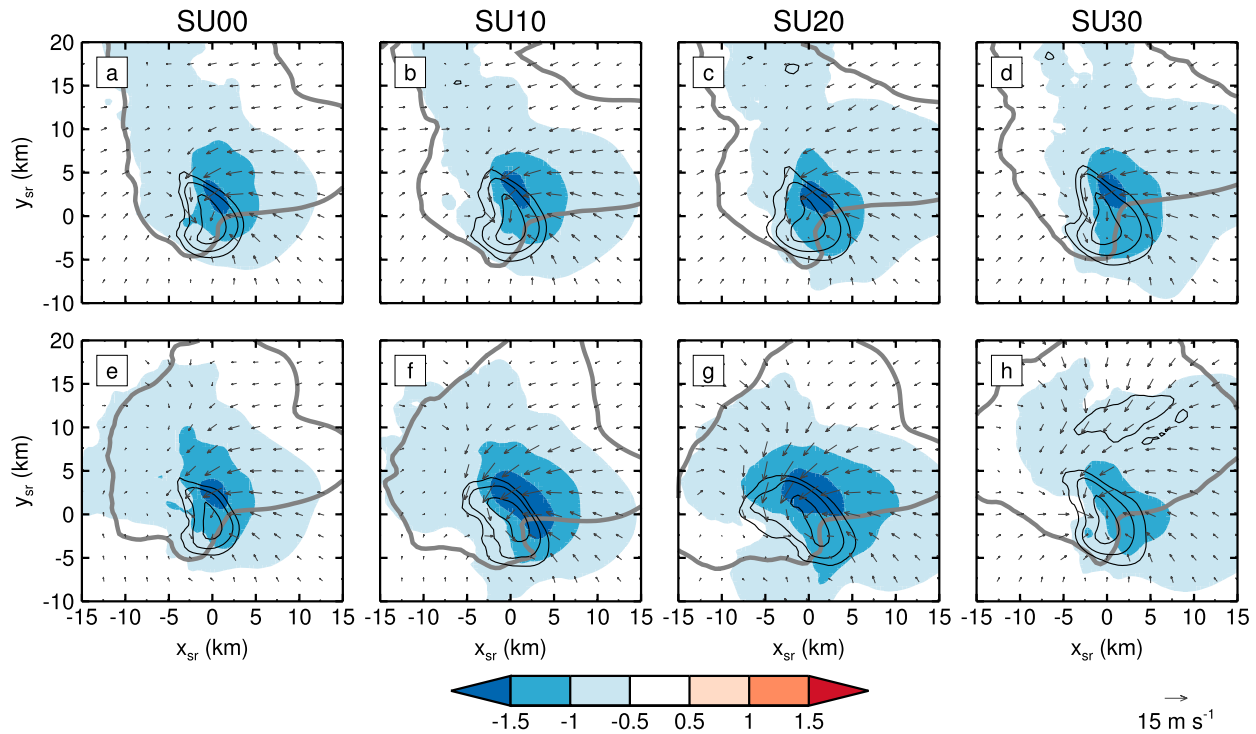


FIG. 12. Composite plan views for (left to right) the SU00, SU10, SU20, and SU30 runs, computed over (a)–(d) $t = 1\text{--}2$ and (e)–(h) $t = 2\text{--}3$ h. Variables shown are 1–3-km average pressure perturbation (colors; hPa), 3–6-km average vertical velocity (thin black contours; 5, 10, and 20 m s^{-1}), 10 mm h^{-1} surface rain-rate outline (thick gray contour), and 1–3-km average perturbation winds (vectors, plotted every 2.5 km; reference vector in bottom right).

The perturbation pressure components were obtained following the method outlined by Coffer and Parker (2015). Unfortunately, the resulting solutions are not unique (they are only determined up to an arbitrary additive constant) and therefore cannot be compared quantitatively. We therefore examined the zonal perturbation pressure gradient accelerations (which are unique), calculated as $(1/\bar{\rho})\partial p'/\partial x$. The results of this analysis (not shown) suggest that the region of negative p' seen in Fig. 12 is primarily associated with the buoyancy and linear-dynamic terms. Both of these tend to become more negative with increasing ULS. More negative p'_b is consistent with the decrease in cold-pool temperatures and a slight increase in thermal buoyancy within the low-level updraft (associated with the enhanced condensation; not shown), which together act to increase $\partial B/\partial z$. More negative p'_{dl} is consistent with a stronger updraft-in-shear effect. However, there is a compensating increase in p'_{dn} associated with enhanced deformation along the stronger cold-pool boundary. The changes in p'_b and p'_{dl} appear to dominate in SU10 and SU20, promoting a net decrease in p' (and enhanced easterly motion) compared to SU00, while the change in p'_{dn} dominates in SU30, promoting a net increase in p' (and reduced easterly motion) compared to SU00.

The calculated perturbation pressure terms also allow us to assess the contribution of dynamic lifting to variations in storm motion between the runs. To this end the linear-, nonlinear-, and total-dynamic VPPGAs were computed as $(1/\bar{\rho})\partial p'/\partial z$. Figure 13 shows horizontal composites of these terms computed over the $0\text{--}6\text{ km}$ layer for a $20 \times 20 \text{ km}^2$ domain centered on the midlevel updraft. As we would expect, an increase in ULS promotes enhanced linear-dynamic accelerations on the upshear and downshear flanks of the updraft. The nonlinear-dynamic acceleration shows a more complex spatial pattern; however, there is a pronounced maximum along the southern flank of the updraft (particularly for $t = 1\text{--}2$ h) associated with the peak in midlevel vorticity (not shown). This feature increases slightly in magnitude and shifts rearward with increasing ULS, presumably reflecting the tilting of an increasing meridional vorticity component above 6 km. The total dynamic VPPGA is maximized along the southeast flank of the updraft and shows a slight increase in magnitude with increasing shear during both the second and third hours of the simulation. In fact, we find that this increase is present as early as $t = 45 \text{ min}$ (not shown), suggesting that enhanced dynamic lifting may contribute to the initial increase in storm motion with increasing ULS.

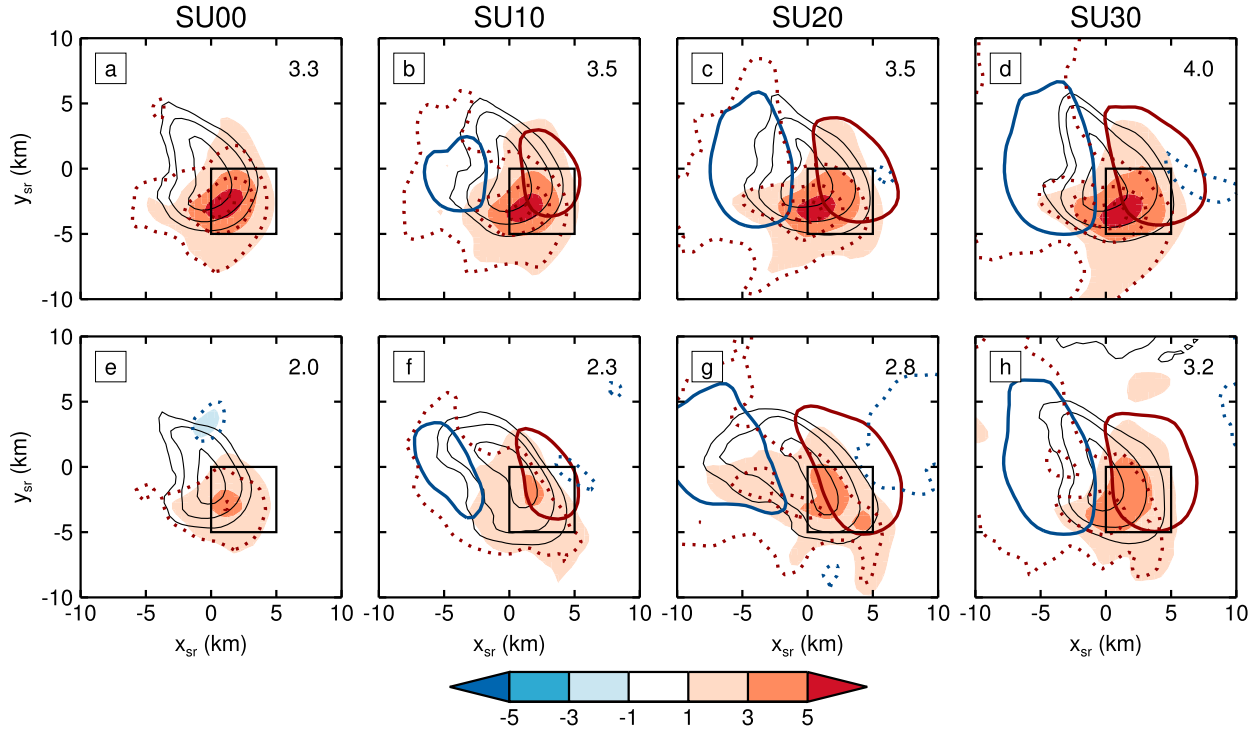


FIG. 13. Composite plan views for (left to right) the SU00, SU10, SU20, and SU30 runs, computed over (a)–(d) $t = 1\text{--}2$ and (e)–(h) $t = 2\text{--}3$ h. Variables shown are 0–6-km dynamic VPPGA (colors; 10^{-2} m s^2) and its linear and nonlinear components (thick solid and dotted lines, respectively; positive in red, negative in blue; same contour levels as color bar), and 3–6-km average vertical velocity (thin black contours; 5, 10, and 20 m s^{-1}). Black box shows the area used to compute the mean dynamic VPPGA given in the top-right corner.

In summary, we find that an increase in 6–12-km shear from 0 to 20 m s^{-1} drives significant changes in simulated supercell characteristics, including wider updrafts, more intense precipitation, and stronger outflow winds. These changes result from an increase in low-level inflow, initially driven by faster storm motion but later enhanced by accelerations associated with a low-level perturbation pressure minimum. The initial increase in storm motion can be explained as a combination of enhanced advection and increased dynamic lifting, although we are unable to quantify the relative contribution of these two effects. However, as the storms mature, it is likely that the stronger cold pools contribute additional accelerations through discrete propagation at the gust front. With a further increase in ULS, from 20 to 30 m s^{-1} , the storm weakens slightly, as the even stronger outflow begins to undercut the updraft.

This final result suggests that there is an optimal ULS magnitude, of around 20 m s^{-1} , for which storm intensity is maximized. However, simulated convective cold pools are remarkably sensitive to other environmental characteristics, such as mixed-layer depth (McCaull and Cohen 2002), and various aspects of the microphysics parameterization (Adler and Droege 2002; van den Heever and Cotton 2004; Cohen and McCaul

2006; Dawson et al. 2010; Morrison and Milbrandt 2011; Van Weverberg et al. 2012). We would therefore expect this optimal ULS threshold to show similar sensitivity. Additional sets of runs performed using (i) a shallower mixed-layer and (ii) the Lin microphysics scheme (Lin et al. 1983; Tao and Simpson 1993) confirm this expectation: in both cases, weaker outflow allows the SU30 storm to remain more intense than its counterparts in the lower-shear runs (not shown). Based on these simulations, we conclude that there is no universal optimal ULS magnitude; however, if the environment is already conducive to the formation of strong cold pools, increasing ULS may ultimately tip the balance in favor of outflow dominance.

b. Variations in upper-level shear distribution and direction

The characteristics of the CONL, CONU, VEER, and BACK runs are illustrated in Fig. 14, which shows plan-view composites for the final simulation hour. The top, middle, and bottom rows show the same fields as in Figs. 5, 10, and 12, respectively, and should be compared with the corresponding plots for SU20. Comparisons with SU20 are also made in Table 3.

We first note that CONL features more intense precipitation, colder cold pools, and stronger outflow than

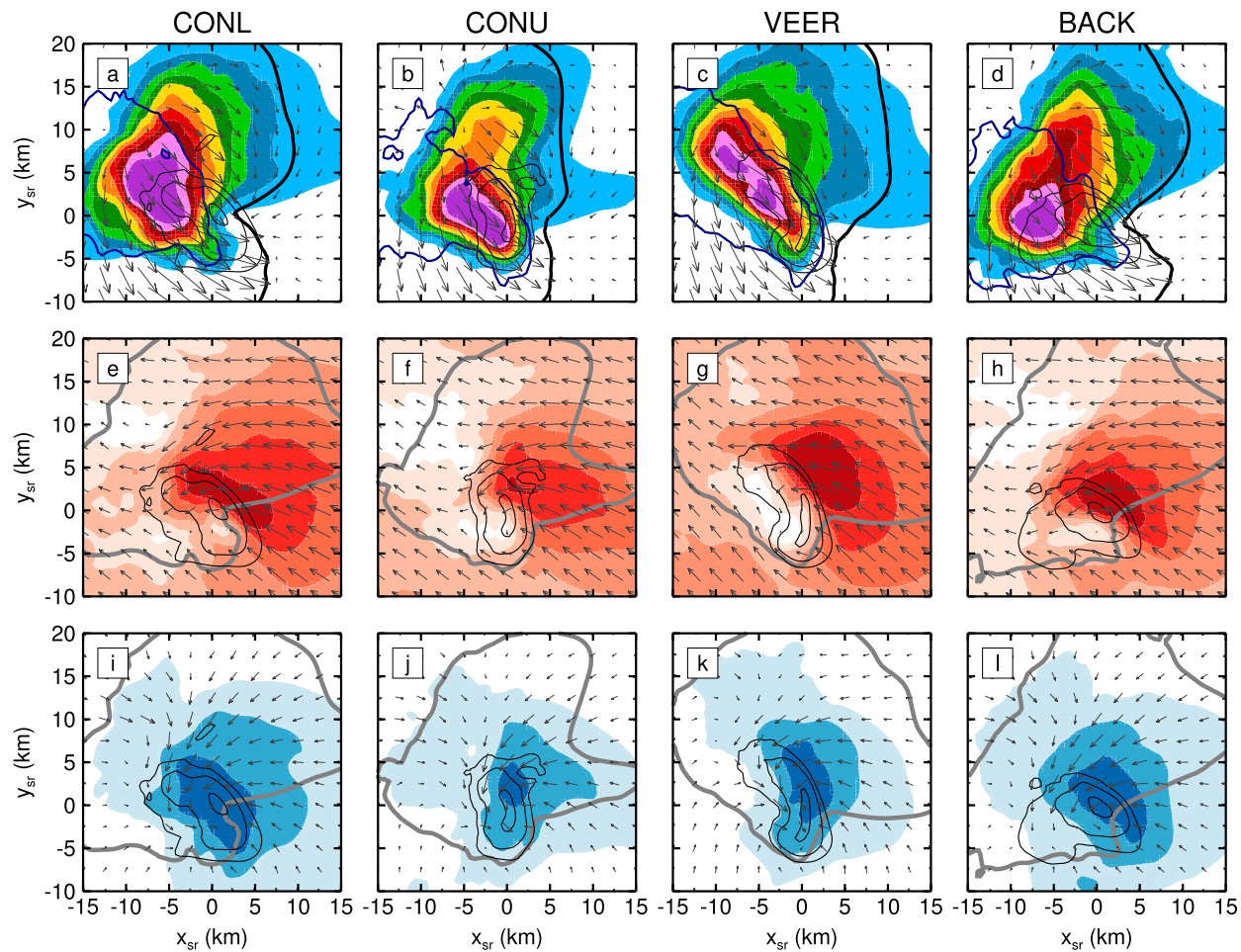


FIG. 14. Composite plan views for (left to right) the CONL, CONU, VEER, and BACK runs, computed over $t = 2\text{--}3$ h. Variables shown in the top, middle, and bottom rows are the same as in Figs. 5, 10, and 12, respectively.

SU20 (Fig. 14a; Table 3). These changes are associated with an increase in storm speed (Table 3) and low-level inflow (Fig. 14e). Storm speed is unchanged in CONU; however, the motion is slightly backed with respect to that of the SU20 storm, resulting in weaker low-level SR flow, less precipitation, and weaker outflow (Figs. 14b,f; Table 3). In both cases, there are again feedbacks on the low-level pressure field and associated perturbation flow that act to amplify initially small differences (Figs. 14i,j). Overall, the CONL and CONU runs are consistent with the results presented in the previous section and highlight the fact that winds in the lower portion of the 6–12-km layer exert greater influence on storm motion than those farther aloft.

The introduction of veering or backing into the ULS profile leads to little change in storm speed (a slight decrease in both cases) but does impact the direction of storm motion (Table 3). As one might expect, the motion vector rotates in the same sense as the shear vector:

clockwise for VEER and counterclockwise for BACK. This influences both the magnitude and direction of the low-level inflow (Figs. 14g,h), which, in turn, modifies the shape of the updraft (by promoting low-level convergence in different storm-relative locations) and the distribution of surface precipitation (Figs. 14c,d). Specifically, in VEER the updraft and precipitation are elongated toward the northwest, while in BACK the updraft is more circular with heavy precipitation concentrated in the storm's rear flank, similar to the HP archetype. This result again stands in contrast to the observations of RS98, which showed veering and backing ULS in HP and LP environments, respectively.

A final conclusion that can be drawn from these simulations is that changing the vertical distribution and direction of ULS has a far smaller impact on storm characteristics than changing the magnitude of ULS. This can be seen by comparing the percentage-change values in columns 2–4 and 5–8 in Table 3. For example,

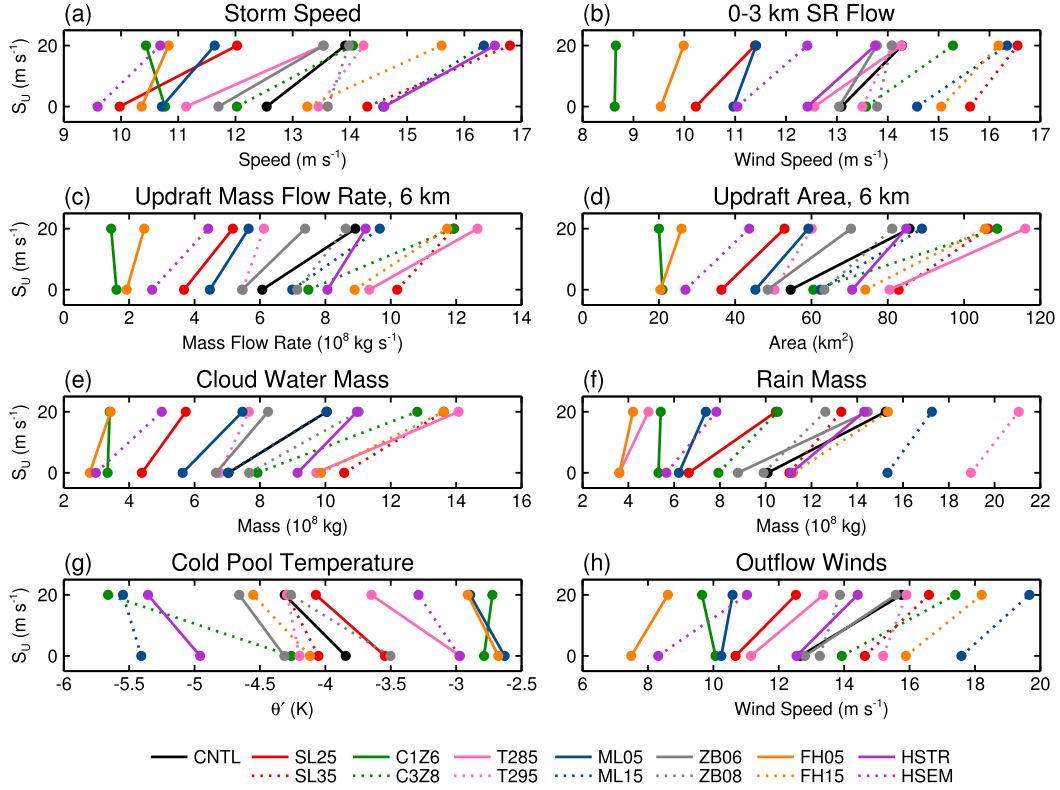


FIG. 15. Summary diagnostics for the control runs (CNTL) and the 14 sensitivity runs listed in Table 2. Variables plotted are (a) storm speed, (b) 0–3-km average storm-relative flow, (c) updraft mass flow rate at $z = 6$ km, (d) updraft area at $z = 6$ km, (e) total cloud water mass, (f) total rain mass, (g) area-averaged surface cold-pool perturbation potential temperature, and (h) area-averaged surface cold-pool (outflow) wind speed. All of these were computed for $t = 1\text{--}3$ h over a 20×20 km 2 moving domain centered on the midlevel updraft centroid. The updraft is defined as the largest contiguous area with $w \geq 5$ m s $^{-1}$ and the surface cold pool is defined as all points with $\theta' \leq -1$ K at $z = 50$ m. The lower and upper circles in each panel show values for the SU00 and SU20 runs, respectively; thus, the lines connecting them indicate the trend associated with increasing ULS.

the swath width for strong winds is 3.5 times larger in SU20 than SU00 but only changes by around 20% in CONL and CONU and 15% in VEER and BACK.

c. Sensitivity to environmental conditions

In this section we seek to address the question of whether variations in ULS impact simulated supercells differently under different environmental conditions. This is achieved through the sensitivity tests listed in Table 2, all of which were performed using the SU00 and SU20 ULS configurations. Figure 15 concisely summarizes the results of these simulations using a selection of relevant diagnostics computed over $t = 1\text{--}3$ h. One can observe some dramatic changes in the storm properties, which are largely consistent with expectations and previous studies. For example, a deeper mixed layer (ML15) favors colder and stronger outflow (McCauley and Cohen 2002), a lower LCL temperature (T285) increases the updraft mass flux (McCauley et al. 2005), and reduced free-tropospheric humidity (FH05) promotes lower

condensate mass (James and Markowski 2010). However, our focus here is not on comparing the storm properties themselves but the trends associated with increasing ULS (i.e., the slope of the lines in Fig. 15).

It is immediately apparent that the effects of ULS (on storm speed, updraft width, outflow strength, etc.) are consistent across almost the full parameter space considered. The magnitude of the change (slope of the lines) varies somewhat—for example, the 6-km updraft area increases much more dramatically for T285 compared to T295—but the direction is the same. The only exception is C1Z6, the configuration with SBCAPE reduced to 1000 J kg $^{-1}$ (and the height of maximum buoyancy reduced to 6 km). In this case, storm motion decreases slightly with increasing ULS, with the other parameters showing either very little change or a change opposite to that in the other runs.

The anomalous nature of C1Z6 can be explained by considering Fig. 16, which shows composite west-to-east vertical cross sections of the SU00 and SU20 runs for this

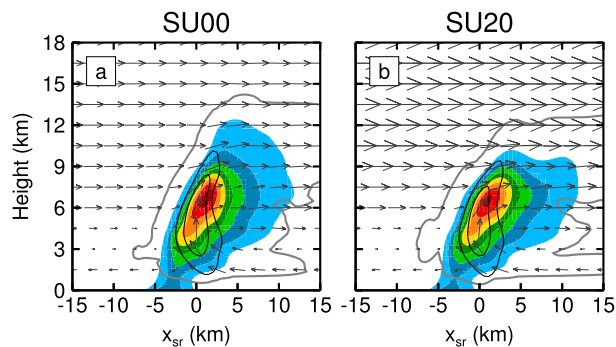


FIG. 16. Composite vertical cross sections for the (a) SU00 and (b) SU20 runs with the C1Z6 sounding, computed over $t = 2\text{--}3$ h. Variables shown are the same as in Fig. 6. Cross sections are taken from west to east at $y_{sr} = 0$ with values averaged over a width of 5 km.

case. In agreement with previous studies, lower CAPE promotes a smaller and shallower supercell with a narrower updraft and reduced condensate mass (Weisman and Klemp 1982; Kirkpatrick et al. 2011). Weaker divergence at cloud top means the storm remains downshear tilted throughout the simulation, even in the absence of ULS (Fig. 16a). With the introduction of moderate ULS, the tilt amplifies while storm-top height decreases (Fig. 16b), similar to what was seen in SU30 (Fig. 6). With less condensate mass above 6 km, the component of storm motion associated with advection is reduced while the contribution of dynamic VPPGAs to propagation is largely unchanged (not shown). Through the chain of processes set out in section 3a, this ultimately leads to less intense surface precipitation, a warmer cold pool, and weaker outflow winds.

In addition to verifying the robustness of our results, these sensitivity tests give context to the simulated changes in storm characteristics. For example, increasing ULS from 0 to 20 m s^{-1} leads to an increase in midlevel updraft area that is comparable to that associated with a 10 m s^{-1} increase in $0\text{--}6\text{-km}$ shear (from 25 to 35 m s^{-1}) or a doubling of CAPE (from 1000 to 2000 J kg^{-1}).

4. Summary and discussion

A series of idealized simulations have been conducted to explore the impact on supercell characteristics of variations in the magnitude, direction, and vertical distribution of upper-level ($6\text{--}12$ km) shear (ULS). A key objective was to test the observationally based hypothesis of RS98 that increasing ULS reduces precipitation formation through enhanced advection of growing hydrometeors away from the updraft, promoting a transition from HP to LP morphology. Our main findings are as follows:

- 1) An increase in the magnitude of ULS promotes faster simulated storm motion. This is initially associated with a combination of enhanced advection (due to stronger upper-level flow) and enhanced propagation (due to stronger dynamic vertical perturbation pressure gradient accelerations). However, subsequent changes in cold-pool characteristics likely contribute to a further increase in propagation later in the storms' evolution.
- 2) As ULS magnitudes increase from 0 to 20 m s^{-1} , storms produce more intense surface precipitation and stronger outflow winds. This trend is associated with an increase in updraft width that promotes enhanced mass flux and condensate production. This in turn can be related to the increase in storm speed via stronger low-level storm-relative (SR) flow. Toward the end of the simulations, inflow is further enhanced through feedbacks that drive a reduction in low-level perturbation pressure.
- 3) When ULS is increased further to 30 m s^{-1} , the above noted trends are reversed as a result of the occurrence of rear-flank gust front surges, which promote intermittent weakening of the low-level mesocyclone. It thus appears that the increase in outflow strength with increasing ULS ultimately acts as a buffer on storm intensity. However, the strong sensitivity of convective cold pools to numerous environmental and model parameters precludes the definition of a universal optimal ULS magnitude.
- 4) As hypothesized by RS98, the increase in upper-level SR flow with increasing ULS initially transports anvil-level hydrometeors farther downstream. However, strengthening cloud-top divergence, associated with the aforementioned increase in updraft mass flux, ultimately reverses this trend in all but the strongest shear case.
- 5) Variations in the vertical distribution of ULS reveal that shear in the lower portion of the $6\text{--}12$ -km layer has a more pronounced impact on storm motion and characteristics than does shear farther aloft.
- 6) The introduction of veering or backing into the ULS profile leads to a slight change in storm direction, which modifies the distribution of the surface precipitation via changes in low-level SR flow and convergence. Specifically, a backing shear vector appears to favor enhanced precipitation in the rear-flank region, while, under veering ULS, the precipitation area is elongated toward the northwest (for approximately westerly storm motion).
- 7) Sensitivity tests reveal that the changes in storm properties (such as updraft area, rain mass, and cold-pool temperature) resulting from the introduction of 20 m s^{-1} of ULS are comparable to those associated with realistic variations in parameters such as CAPE, mixed-layer depth, and $0\text{--}6\text{-km}$ shear.

Clearly, RS98's hypothesis is not supported by our results. Rather than limiting the growth of hydrometeors, the introduction of ULS into our simulations actually leads to more intense precipitation via an increase in storm motion and low-level inflow. Thus, we observe a transition to a more HP-like structure with increasing ULS, the precise opposite of what RS98 predicted.

Can we reconcile these disparate findings? One possibility is that the differences in ULS between CL, LP, and HP supercells observed by RS98 are simply a by-product of the environments that favor these morphologies. For example, it has been observed that, in the Great Plains, LP storms tend to form in close proximity to the dryline (Bluestein and Parks 1983). Strong drylines typically form ahead of an upper-level short-wave trough (Schultz et al. 2007), and jet maxima, associated with these troughs, are well known to favor convective development through induced secondary circulations (e.g., Uccellini and Johnson 1979). Thus, it may be that the stronger ULS in LP-supercell environments reflects a tendency for stronger upper-level flow in the vicinity of convectively active drylines.

An alternative explanation is the high relative humidity of our idealized soundings compared with those observed by RS98. As noted in section 2b, such moist environmental conditions were required to produce sustained convection, which is most likely due to our use of a warm-bubble initialization (Naylor and Gilmore 2012). It is possible that the impact of increasing ULS is reversed in drier environments; that is, stronger shear promotes a reduction in storm speed, leading ultimately to a more LP-like (or, at least, less HP like) structure (similar to the low-CAPE case, C1Z6). The fact that the trends in storm characteristics associated with increasing ULS are reduced in the slightly drier FH05 simulations (Fig. 15) lends some support to this hypothesis. However, further experimentation is needed to determine whether the trends are actually reversed in even drier environments.

A final possibility that must be entertained is that our simulations fail to accurately represent relevant dynamical and/or microphysical processes that govern the evolution of real supercells. Recent work has shown that high-resolution numerical weather prediction models tend to move storms too fast (e.g., Yussouf et al. 2015; Snook et al. 2016; Supinie et al. 2016). This has been hypothesized to be the result of assimilation errors (Yussouf et al. 2015) or cold-pool biases (Supinie et al. 2016); however, it may be that the influence of upper-level winds on storm motion is exaggerated. In particular, the absence of resolved turbulent entrainment and associated excessive updraft velocities (e.g., Lebo and Morrison 2015) may promote both faster advection, via enhanced condensate mass at upper levels, and faster propagation, via stronger

linear-dynamic forcing. Such a bias could explain the disagreement between our results and the observations, which mostly suggest that winds above 6 km do not influence supercell motion (e.g., Bunkers et al. 2014). Another aspect of model fidelity that should be considered is the ability to represent the full supercell spectrum. It is notable that all of the supercells simulated here, together with the vast majority of those in past idealized modeling studies, most closely resemble the HP archetype, with heavy precipitation concentrated to the rear of the mesocyclone. While this tendency may again be a consequence of overly moist input soundings, it could also reflect a systematic model bias, perhaps related to the representation of certain microphysical processes.

The disparate hazards associated with LP, HP, and CL supercells provide strong motivation for continued research into the environmental factors that distinguish these morphologies. In the near term, we intend to repeat the primary simulations presented herein using drier input soundings (combined with a more sophisticated method of storm initialization) to provide a more appropriate comparison with the observations of RS98. Further investigation into the impact of variations in the vertical profile of relative humidity on simulated supercells is also required. From an operational perspective, there is a need to ascertain whether convection-permitting numerical weather prediction models can reliably forecast supercell morphology and, if so, at what lead time. A pertinent question is whether the above-noted overrepresentation of HP storms in idealized simulations also occurs in full-physics operational-type runs. All of these efforts must be supported by continued work on model verification, particularly with regard to precipitation microphysics. Finally, we suggest that, given the ever-expanding archives of radar and near-storm environment data for severe weather events (e.g., Thompson et al. 2012), the time is right to revisit RS98's hypothesis from an observational standpoint.

Acknowledgments. RAW was funded by Australian Research Council Linkage Project Grant LP130100679. Simulations were performed on the National Computing Infrastructure's Raijin supercomputer. We would like to acknowledge Brice Coffer, for invaluable assistance with the pressure perturbation analysis, and Dave Kinniburgh and Paul Markowski, for additional useful discussions on this subject. We also thank George Bryan, for providing and maintaining CM1, and Rich Thompson, for furnishing us with the supercell proximity dataset. Finally, we gratefully acknowledge Matt Bunkers and three anonymous reviewers for their detailed and insightful comments on an earlier draft of this manuscript.

APPENDIX

Construction of Environmental Profiles

a. Thermodynamic profiles

The base-state thermodynamic soundings used in our simulations were all created following the approach of McCaul and Weisman (2001). Three layers—a mixed layer, free troposphere, and stratosphere—are specified using the first 10 parameters listed in Table 1. The mixed layer is defined by its depth, z_{ml} ; a prescribed potential temperature lapse rate, γ_{ml} ; the air properties at its top (temperature, T_{ml} ; relative humidity, H_{ml} ; and pressure, p_{ml}); and the assumption of constant equivalent potential temperature. The pressure at the mixed-layer top is selected to give a surface pressure of approximately 1000 hPa in all experiments. Profiles of potential temperature and water vapor mixing ratio over this layer are determined by integrating down from z_{ml} to the surface.

Above the mixed-layer top, McCaul and Weisman (2001) assumed constant relative humidity. Improving on this very simple approach, we use the following equation to specify H between z_{ml} and z_{tp} , the height of the tropopause:

$$H(z) = H_{\text{ml}} - (H_{\text{ml}} - H_{\text{tp}}) \left(\frac{z - z_{\text{ml}}}{z_{\text{tp}} - z_{\text{ml}}} \right)^F. \quad (\text{A1})$$

Here, H_{tp} is the humidity at the tropopause (25% in all our simulations) and F is a factor that controls the rate of decrease with altitude. In most runs, we take $F = 1$ so that the humidity decreases linearly. A profile of thermal buoyancy is then specified as

$$B(z) = E \frac{z - z_{\text{ml}}}{(z_B - z_{\text{ml}})^2} \exp\left(-\frac{z - z_{\text{ml}}}{z_B - z_{\text{ml}}}\right), \quad (\text{A2})$$

where E is the SBCAPE and z_B is the height of maximum buoyancy. From this and the properties of a surface parcel lifted dry-adiabatically to its LCL and then pseudoadiabatically to height z , the virtual temperature, T_v , of the environment can be derived by rearranging the equation for buoyancy:

$$B = g \frac{T_{v,p} - T_{v,e}}{T_{v,e}}, \quad (\text{A3})$$

where g is the acceleration due to gravity and the subscripts p and e indicate the parcel and environment, respectively. The environmental potential temperature and mixing ratio are then obtained iteratively from T_v and H .

Above the tropopause, the temperature and mixing ratio are taken to be constant. This truncates the buoyancy

profile, resulting in CAPE that is lower than the specified value. To obtain the correct value, the calculations above the mixed layer are repeated iteratively, with the buoyancy profile at step n scaled by E/E_{n-1} . For the values of SBCAPE considered here, 5–10 iterations were required to obtain a precision of $\pm 0.5 \text{ J kg}^{-1}$.

b. Wind profiles

The quarter-circle, straight, and semicircle hodographs used to define shear over the 0–6-km layer have been used extensively in previous supercell simulations (e.g., Weisman and Rotunno 2000), so their construction will not be detailed here. Rather, we focus on the different upper-level (6–12 km) wind profiles employed. With unidirectional ULS, the wind components are given by

$$\begin{aligned} u(z) &= u_L + S_U f(Z) \\ v(z) &= v_L, \end{aligned} \quad (\text{A4})$$

where u_L and v_L are the wind components at $z = z_L$, S_U is the hodograph length in the layer, $Z = (z - z_L)/z_U$ is the fractional height in the layer, and

$$f(Z) = \begin{cases} Z & \text{for uniform shear} \\ \sin(\pi Z/2) & \text{for lower-concentrated shear} \\ 1 - \cos(\pi Z/2) & \text{for upper-concentrated shear} \end{cases}. \quad (\text{A5})$$

In cases where the shear vector rotates through an angle ϕ_U over the layer, the wind components are instead given by

$$\begin{aligned} u(z) &= u_L + \frac{S_U}{\phi_U} \sin(\phi_U Z) \\ v(z) &= v_L - \frac{S_U}{\phi_U} [1 - \cos(\phi_U Z)], \end{aligned} \quad (\text{A6})$$

where ϕ_U is expressed in radians and is positive for clockwise rotation (veering). The values of the parameters z_L , z_U , S_L , S_U , and ϕ_U are given in Table 1.

REFERENCES

- Adlerman, E. J., and K. K. Droegemeier, 2002: The sensitivity of numerically simulated cyclic mesocyclogenesis to variations in model physical and computational parameters. *Mon. Wea. Rev.*, **130**, 2671–2691, doi:10.1175/1520-0493(2002)130<2671:TSONSC>2.0.CO;2.
 Beatty, K., E. Rasmussen, and J. Straka, 2008: The supercell spectrum. Part I: A review of research related to supercell precipitation morphology. *Electron. J. Severe Storms Meteor.*, **3**(4). [Available online at <http://www.ejssm.org/ojs/index.php/ejssm/article/viewArticle/44/>.]
 —, E. N. Rasmussen, J. M. Straka, and L. R. Lemon, 2009: The supercell spectrum. Part II: A semi-objective method for radar

- classification of supercell type. *Electron. J. Severe Storms Meteor.*, **4** (1). [Available online at <http://ejssm.org/ojs/index.php/ejssm/article/viewArticle/45>.]
- Bluestein, H. B., 1984: Further examples of low-precipitation severe thunderstorms. *Mon. Wea. Rev.*, **112**, 1885–1888, doi:[10.1175/1520-0493\(1984\)112<1885:FEOLPS>2.0.CO;2](https://doi.org/10.1175/1520-0493(1984)112<1885:FEOLPS>2.0.CO;2).
- , and C. R. Parks, 1983: A synoptic and photographic climatology of low-precipitation severe thunderstorms in the southern plains. *Mon. Wea. Rev.*, **111**, 2034–2046, doi:[10.1175/1520-0493\(1983\)111<2034:ASAPCO>2.0.CO;2](https://doi.org/10.1175/1520-0493(1983)111<2034:ASAPCO>2.0.CO;2).
- Brooks, H. E., C. A. Doswell III, and R. B. Wilhelmson, 1994: The role of midtropospheric winds in the evolution and maintenance of low-level mesocyclones. *Mon. Wea. Rev.*, **122**, 126–136, doi:[10.1175/1520-0493\(1994\)122<0126:TROMWI>2.0.CO;2](https://doi.org/10.1175/1520-0493(1994)122<0126:TROMWI>2.0.CO;2).
- Browning, K. A., 1964: Airflow and precipitation trajectories within severe local storms which travel to the right of the winds. *J. Atmos. Sci.*, **21**, 634–639, doi:[10.1175/1520-0469\(1964\)021<0634:AAPTWS>2.0.CO;2](https://doi.org/10.1175/1520-0469(1964)021<0634:AAPTWS>2.0.CO;2).
- Bryan, G. H., 2016: The governing equations for CM1. National Center for Atmospheric Research Tech. Rep., 17 pp. [Available online at http://www2.mmm.ucar.edu/people/bryan/cm1/cm1_equations.pdf.]
- , and J. M. Fritsch, 2002: A benchmark simulation for moist nonhydrostatic numerical models. *Mon. Wea. Rev.*, **130**, 2917–2928, doi:[10.1175/1520-0493\(2002\)130<2917:ABSMN>2.0.CO;2](https://doi.org/10.1175/1520-0493(2002)130<2917:ABSMN>2.0.CO;2).
- , J. C. Wyngaard, and J. M. Fritsch, 2003: Resolution requirements for the simulation of deep moist convection. *Mon. Wea. Rev.*, **131**, 2394–2416, doi:[10.1175/1520-0493\(2003\)131<2394:RRFTSO>2.0.CO;2](https://doi.org/10.1175/1520-0493(2003)131<2394:RRFTSO>2.0.CO;2).
- Bunkers, M. J., 2010: How midlevel horizontal humidity gradients affect simulated storm morphology. *25th Conf. on Severe Local Storms*, Denver, CO, Amer. Meteor. Soc., P7.1. [Available online at <https://ams.confex.com/ams/25SLS/webprogram/Paper175623.html>.]
- , B. A. Klimowski, J. W. Zeitler, R. L. Thompson, and M. L. Weisman, 2000: Predicting supercell motion using a new hodograph technique. *Wea. Forecasting*, **15**, 61–79, doi:[10.1175/1520-0434\(2000\)015<0061:PSMUAN>2.0.CO;2](https://doi.org/10.1175/1520-0434(2000)015<0061:PSMUAN>2.0.CO;2).
- , D. A. Barber, R. L. Thompson, R. Edwards, and J. Garner, 2014: Choosing a universal mean wind for supercell motion prediction. *J. Oper. Meteor.*, **2**, 115–129, doi:[10.15191/nwajom.2014.0211](https://doi.org/10.15191/nwajom.2014.0211).
- Coffer, B. E., and M. D. Parker, 2015: Impacts of increasing low-level shear on supercells during the early evening transition. *Mon. Wea. Rev.*, **143**, 1945–1969, doi:[10.1175/MWR-D-14-00328.1](https://doi.org/10.1175/MWR-D-14-00328.1).
- Cohen, C., and E. W. McCaul Jr., 2006: The sensitivity of simulated convective storms to variations in prescribed single-moment microphysics parameters that describe particle distributions, sizes, and numbers. *Mon. Wea. Rev.*, **134**, 2547–2565, doi:[10.1175/MWR3195.1](https://doi.org/10.1175/MWR3195.1).
- Davies, J. M., 1998: On supercell motion in weaker wind environments. Preprints, *19th Conf. on Severe Local Storms*, Minneapolis, MN, Amer. Meteor. Soc., 685–688.
- , and R. H. Johns, 1993: Some wind and instability parameters associated with strong and violent tornadoes. Part I: Wind shear and helicity. *The Tornado: Its Structure, Dynamics, Prediction, and Hazards, Geophys. Monogr.*, Vol. 79, Amer. Geophys. Union, 573–582.
- Davies-Jones, R., 2002: Linear and nonlinear propagation of supercell storms. *J. Atmos. Sci.*, **59**, 3178–3205, doi:[10.1175/1520-0469\(2003\)059<3178:LANPOS>2.0.CO;2](https://doi.org/10.1175/1520-0469(2003)059<3178:LANPOS>2.0.CO;2).
- , 2003: An expression for effective buoyancy in surroundings with horizontal density gradients. *J. Atmos. Sci.*, **60**, 2922–2925, doi:[10.1175/1520-0469\(2003\)060<2922:AEFEBI>2.0.CO;2](https://doi.org/10.1175/1520-0469(2003)060<2922:AEFEBI>2.0.CO;2).
- Dawson, D. T., II, M. Xue, J. A. Milbrandt, and M. Yau, 2010: Comparison of evaporation and cold pool development between single-moment and multimoment bulk microphysics schemes in idealized simulations of tornadic thunderstorms. *Mon. Wea. Rev.*, **138**, 1152–1171, doi:[10.1175/2009MWR2956.1](https://doi.org/10.1175/2009MWR2956.1).
- Deardorff, J. W., 1980: Stratocumulus-capped mixed layers derived from a three-dimensional model. *Bound.-Layer Meteor.*, **18**, 495–527, doi:[10.1007/BF00119502](https://doi.org/10.1007/BF00119502).
- Doswell, C. A., III, and P. M. Markowski, 2004: Is buoyancy a relative quantity? *Mon. Wea. Rev.*, **132**, 853–863, doi:[10.1175/1520-0493\(2004\)132<0853:IBARQ>2.0.CO;2](https://doi.org/10.1175/1520-0493(2004)132<0853:IBARQ>2.0.CO;2).
- , A. R. Moller, and R. Przybylinski, 1990: A unified set of conceptual models for variations on the supercell theme. *Preprints, 16th Conf. on Severe Local Storms*, Kananaskis Park, AB, Canada, Amer. Meteor. Soc., 40–45.
- Grant, L. D., and S. C. Van den Heever, 2014: Microphysical and dynamical characteristics of low-precipitation and classic supercells. *J. Atmos. Sci.*, **71**, 2604–2624, doi:[10.1175/JAS-D-13-0261.1](https://doi.org/10.1175/JAS-D-13-0261.1).
- Hastings, R., and Y. Richardson, 2016: Long-term morphological changes in simulated supercells following mergers with nascent supercells in directionally varying shear. *Mon. Wea. Rev.*, **144**, 471–499, doi:[10.1175/MWR-D-15-0193.1](https://doi.org/10.1175/MWR-D-15-0193.1).
- James, R. P., and P. M. Markowski, 2010: A numerical investigation of the effects of dry air aloft on deep convection. *Mon. Wea. Rev.*, **138**, 140–161, doi:[10.1175/2009MWR3018.1](https://doi.org/10.1175/2009MWR3018.1).
- Jeevanjee, N., and D. M. Romps, 2016: Effective buoyancy at the surface and aloft. *Quart. J. Roy. Meteor. Soc.*, **142**, 811–820, doi:[10.1002/qj.2683](https://doi.org/10.1002/qj.2683).
- Kirkpatrick, C., E. W. McCaul Jr., and C. Cohen, 2011: Sensitivities of simulated convective storms to environmental CAPE. *Mon. Wea. Rev.*, **139**, 3514–3532, doi:[10.1175/2011MWR3631.1](https://doi.org/10.1175/2011MWR3631.1).
- Klemp, J. B., and R. B. Wilhelmson, 1978: The simulation of three-dimensional convective storm dynamics. *J. Atmos. Sci.*, **35**, 1070–1096, doi:[10.1175/1520-0469\(1978\)035<1070:TSOTDC>2.0.CO;2](https://doi.org/10.1175/1520-0469(1978)035<1070:TSOTDC>2.0.CO;2).
- Lakshmanan, V., B. Herzog, and D. Kingfield, 2015: A method for extracting postevent storm tracks. *J. Appl. Meteor. Climatol.*, **54**, 451–462, doi:[10.1175/JAMC-D-14-0132.1](https://doi.org/10.1175/JAMC-D-14-0132.1).
- Lebo, Z., and H. Morrison, 2015: Effects of horizontal and vertical grid spacing on mixing in simulated squall lines and implications for convective strength and structure. *Mon. Wea. Rev.*, **143**, 4355–4375, doi:[10.1175/MWR-D-15-0154.1](https://doi.org/10.1175/MWR-D-15-0154.1).
- Lemon, L. R., and C. A. Doswell III, 1979: Severe thunderstorm evolution and mesocyclone structure as related to tornadogenesis. *Mon. Wea. Rev.*, **107**, 1184–1197, doi:[10.1175/1520-0493\(1979\)107<1184:STEAMS>2.0.CO;2](https://doi.org/10.1175/1520-0493(1979)107<1184:STEAMS>2.0.CO;2).
- Lin, Y.-L., R. D. Farley, and H. D. Orville, 1983: Bulk parameterization of the snow field in a cloud model. *J. Climate Appl. Meteor.*, **22**, 1065–1092, doi:[10.1175/1520-0450\(1983\)022<1065:BPOTSF>2.0.CO;2](https://doi.org/10.1175/1520-0450(1983)022<1065:BPOTSF>2.0.CO;2).
- Loftus, A. M., D. B. Weber, and C. A. Doswell III, 2008: Parameterized mesoscale forcing mechanisms for initiating numerically simulated isolated multicellular convection. *Mon. Wea. Rev.*, **136**, 2408–2421, doi:[10.1175/2007MWR2133.1](https://doi.org/10.1175/2007MWR2133.1).
- Markowski, P., and Y. Richardson, 2010: *Mesoscale Meteorology in Midlatitudes*. Wiley-Blackwell, 407 pp.
- , and —, 2014: The influence of environmental low-level shear and cold pools on tornadogenesis: Insights from idealized simulations. *J. Atmos. Sci.*, **71**, 243–275, doi:[10.1175/JAS-D-13-0159.1](https://doi.org/10.1175/JAS-D-13-0159.1).

- McCaull, E. W., Jr., and M. L. Weisman, 2001: The sensitivity of simulated supercell structure and intensity to variations in the shapes of environmental buoyancy and shear profiles. *Mon. Wea. Rev.*, **129**, 664–687, doi:10.1175/1520-0493(2001)129<0664:TSOSS>2.0.CO;2.
- , and C. Cohen, 2002: The impact on simulated storm structure and intensity of variations in the mixed layer and moist layer depths. *Mon. Wea. Rev.*, **130**, 1722–1748, doi:10.1175/1520-0493(2002)130<1722:TSOSS>2.0.CO;2.
- , and —, 2004: The initiation, longevity, and morphology of simulated convective storms as a function of free-tropospheric relative humidity. *11th Conf. on Aviation, Range, and Aerospace/22nd Conf. on Severe Local Storms*, Hyannis, MA, Amer. Meteor. Soc., 8A.5. [Available online at <https://ams.confex.com/ams/11aram22sls/webprogram/Paper81251.html>.]
- , —, and C. Kirkpatrick, 2005: The sensitivity of simulated storm structure, intensity, and precipitation efficiency to environmental temperature. *Mon. Wea. Rev.*, **133**, 3015–3037, doi:10.1175/MWR3015.1.
- Moller, A. R., C. A. Doswell III, and R. Przybylinski, 1990: High precipitation supercells: A conceptual model and documentation. *Preprints, 16th Conf. on Severe Local Storms*, Kananaskis Park, AB, Canada, Amer. Meteor. Soc., 52–57.
- , —, M. P. Foster, and G. R. Woodall, 1994: The operational recognition of supercell thunderstorm environments and storm structures. *Wea. Forecasting*, **9**, 327–347, doi:10.1175/1520-0434(1994)009<0327:TOROST>2.0.CO;2.
- Morrison, H., 2016a: Impacts of updraft size and dimensionality on the perturbation pressure and vertical velocity in cumulus convection. Part I: Simple, generalized analytic solutions. *J. Atmos. Sci.*, **73**, 1441–1454, doi:10.1175/JAS-D-15-0040.1.
- , 2016b: Impacts of updraft size and dimensionality on the perturbation pressure and vertical velocity in cumulus convection. Part II: Comparison of theoretical and numerical solutions and fully dynamical simulations. *J. Atmos. Sci.*, **73**, 1455–1480, doi:10.1175/JAS-D-15-0041.1.
- , and J. Milbrandt, 2011: Comparison of two-moment bulk microphysics schemes in idealized supercell thunderstorm simulations. *Mon. Wea. Rev.*, **139**, 1103–1130, doi:10.1175/2010MWR3433.1.
- , J. Curry, and V. Khvorostyanov, 2005: A new double-moment microphysics parameterization for application in cloud and climate models. Part I: Description. *J. Atmos. Sci.*, **62**, 1665–1677, doi:10.1175/JAS3446.1.
- Naylor, J., and M. S. Gilmore, 2012: Convective initiation in an idealized cloud model using an updraft nudging technique. *Mon. Wea. Rev.*, **140**, 3699–3705, doi:10.1175/MWR-D-12-00163.1.
- Nelson, S. P., 1987: The hybrid multicellular-supercellular storm—An efficient hail producer. Part II. General characteristics and implications for hail growth. *J. Atmos. Sci.*, **44**, 2060–2073, doi:10.1175/1520-0469(1987)044<2060:THMSEH>2.0.CO;2.
- Nowotarski, C. J., P. M. Markowski, and Y. P. Richardson, 2011: The characteristics of numerically simulated supercell storms situated over statically stable boundary layers. *Mon. Wea. Rev.*, **139**, 3139–3162, doi:10.1175/MWR-D-10-05087.1.
- Parker, M. D., 2010: Relationship between system slope and updraft intensity in squall lines. *Mon. Wea. Rev.*, **138**, 3572–3578, doi:10.1175/2010MWR3441.1.
- Petch, J., 2006: Sensitivity studies of developing convection in a cloud-resolving model. *Quart. J. Roy. Meteor. Soc.*, **132**, 345–358, doi:10.1256/qj.05.71.
- Ramsay, H. A., and C. A. Doswell III, 2005: A sensitivity study of hodograph-based methods for estimating supercell motion. *Wea. Forecasting*, **20**, 954–970, doi:10.1175/WAF889.1.
- Rasmussen, E. N., and D. O. Blanchard, 1998: A baseline climatology of sounding-derived supercell and tornado forecast parameters. *Wea. Forecasting*, **13**, 1148–1164, doi:10.1175/1520-0434(1998)013<1148:ABCOSD>2.0.CO;2.
- , and J. M. Straka, 1998: Variations in supercell morphology. Part I: Observations of the role of upper-level storm-relative flow. *Mon. Wea. Rev.*, **126**, 2406–2421, doi:10.1175/1520-0493(1998)126<2406:VISMPI>2.0.CO;2.
- Rotunno, R., and J. B. Klemp, 1982: The influence of the shear-induced pressure gradient on thunderstorm motion. *Mon. Wea. Rev.*, **110**, 136–151, doi:10.1175/1520-0493(1982)110<0136:TIOTSI>2.0.CO;2.
- , and —, 1985: On the rotation and propagation of simulated supercell thunderstorms. *J. Atmos. Sci.*, **42**, 271–292, doi:10.1175/1520-0469(1985)042<0271:OTRAPO>2.0.CO;2.
- Schultz, D. M., C. C. Weiss, and P. M. Hoffman, 2007: The synoptic regulation of dryline intensity. *Mon. Wea. Rev.*, **135**, 1699–1709, doi:10.1175/MWR3376.1.
- Snook, N., Y. Jung, J. Brotzge, B. Putnam, and M. Xue, 2016: Prediction and ensemble forecast verification of hail in the supercell storms of 20 May 2013. *Wea. Forecasting*, **31**, 811–825, doi:10.1175/WAF-D-15-0152.1.
- Supinie, T. A., N. Yussouf, Y. Jung, M. Xue, and J. Cheng, 2016: An evaluation of the utility of the WRT phased array radar observations as compared to WSR-88D in the analyses and forecasts of a tornadic supercell storm. *28th Conf. on Severe Local Storms*, Portland, OR, Amer. Meteor. Soc., 12B.3. [Available online at <https://ams.confex.com/ams/28SLS/webprogram/Paper301958.html>.]
- Tao, W.-K., and J. Simpson, 1993: The Goddard Cumulus Ensemble Model. Part I: Model description. *Terr. Atmos. Oceanic Sci.*, **4**, 35–72, doi:10.3319/TAO.1993.4.1.35(A).
- Thompson, R. L., C. M. Mead, and R. Edwards, 2007: Effective storm-relative helicity and bulk shear in supercell thunderstorm environments. *Wea. Forecasting*, **22**, 102–115, doi:10.1175/WAF969.1.
- , B. T. Smith, J. S. Grams, A. R. Dean, and C. Broyles, 2012: Convective modes for significant severe thunderstorms in the contiguous United States. Part II: Supercell and QLCS tornado environments. *Wea. Forecasting*, **27**, 1136–1154, doi:10.1175/WAF-D-11-00116.1.
- Uccellini, L. W., and D. R. Johnson, 1979: The coupling of upper and lower tropospheric jet streaks and implications for the development of severe convective storms. *Mon. Wea. Rev.*, **107**, 682–703, doi:10.1175/1520-0493(1979)107<0682:TCOUAL>2.0.CO;2.
- Van den Heever, S. C., and W. R. Cotton, 2004: The impact of hail size on simulated supercell storms. *J. Atmos. Sci.*, **61**, 1596–1609, doi:10.1175/1520-0469(2004)061<1596:TIOHSO>2.0.CO;2.
- Van Weverberg, K., A. M. Vogelmann, H. Morrison, and J. A. Milbrandt, 2012: Sensitivity of idealized squall-line simulations to the level of complexity used in two-moment bulk microphysics schemes. *Mon. Wea. Rev.*, **140**, 1883–1907, doi:10.1175/MWR-D-11-00120.1.
- Verelle, A., D. Ricard, and C. Lac, 2015: Sensitivity of high-resolution idealized simulations of thunderstorms to horizontal resolution and turbulence parametrization. *Quart. J. Roy. Meteor. Soc.*, **141**, 433–448, doi:10.1002/qj.2363.
- Weisman, M. L., and J. B. Klemp, 1982: The dependence of numerically simulated convective storms on vertical wind shear and buoyancy. *Mon. Wea. Rev.*, **110**, 504–520, doi:10.1175/1520-0493(1982)110<0504:TDONSC>2.0.CO;2.

- , and —, 1984: The structure and classification of numerically simulated convective storms in directionally varying wind shears. *Mon. Wea. Rev.*, **112**, 2479–2498, doi:[10.1175/1520-0493\(1984\)112<2479:TSACON>2.0.CO;2](https://doi.org/10.1175/1520-0493(1984)112<2479:TSACON>2.0.CO;2).
- , and R. Rotunno, 2000: The use of vertical wind shear versus helicity in interpreting supercell dynamics. *J. Atmos. Sci.*, **57**, 1452–1472, doi:[10.1175/1520-0469\(2000\)057<1452:TUVWS>2.0.CO;2](https://doi.org/10.1175/1520-0469(2000)057<1452:TUVWS>2.0.CO;2).
- Yussouf, N., D. C. Dowell, L. J. Wicker, K. H. Knopfmeier, and D. M. Wheatley, 2015: Storm-scale data assimilation and ensemble forecasts for the 27 April 2011 severe weather outbreak in Alabama. *Mon. Wea. Rev.*, **143**, 3044–3066, doi:[10.1175/MWR-D-14-00268.1](https://doi.org/10.1175/MWR-D-14-00268.1).
- Zeitler, J. W., and M. J. Bunkers, 2005: Operational forecasting of supercell motion: Review and case studies using multiple datasets. *Natl. Wea. Dig.*, **29** (1), 81–97.